Quasigeostrophic Dynamics of the Western Boundary Current

PAVEL S. BERLOFF AND JAMES C. MCWILLIAMS

Institute of Geophysics and Planetary Physics, University of California, Los Angeles, Los Angeles, California

(Manuscript received 2 April 1998, in final form 11 December 1998)

ABSTRACT

A local model is used to investigate the dynamics of the western boundary current in a midlatitude, wind-driven gyre. This current is important for the gyre as a whole, and its local instability is correlated with structural changes of the separated eastward jet and the interior gyres. In particular, the eastward jet can be disrupted and broadened in the regime with a strong, local instability in the western boundary current. Such a regime occurs with a no-slip lateral boundary condition. Alternatively, in the absence of local instability, the eastward jet is narrow and penetrates farther in the basin interior. This behavior is typical with free-slip boundary condition.

Both the linear stability and nonlinear time-dependent behavior of the western boundary current are analyzed for a wide range of parameters. The current loses stability at moderate Reynolds numbers, and the stability threshold strongly depends upon the vertical stratification profile. The nonlinear time-dependent flow contains well-defined mesoscale eddies with adjacent meanders. The finite amplitude dynamics is fundamentally different in the no-slip and free-slip situations, because the free-slip boundary substantially stabilizes the flow. It is shown that fluctuations in nonlinear regime are rather different from the linearly unstable modes. Multiple stable equilibria are also found.

1. Introduction

In this paper we focus on the fundamental dynamics of a midlatitude western boundary current (WBC), such as the Gulf Stream, Kuroshio, Somali, East Australian, and Brazil currents. We use an idealized local model of the WBC in a north–south channel. We explore dynamics of the model for a wide range of parameters, including relatively large values of the Reynolds number, Re. In the introduction we outline the background, pose the problem, and formulate the numerical model. In section 2 we analyze solutions of the wind-driven, basin-scale, double-gyre circulation with and without instabilities of the WBCs. In section 3 we solve for linear stability of the WBC. Section 4 focuses on nonlinear dynamics of the WBC. Conclusions follow in section 5.

a. Background

Correct modeling of the oceanic lateral boundary layer is a very difficult problem. Behavior of the boundary layer at even moderate values of Re is poorly known; there are strong computational barriers to achieving the large values of Re typical for the ocean. Also, the common practice of using a vertical sidewall and an associated stress boundary condition gives considerable computational convenience, but such a boundary is artificial in comparison with a shoaling bottom at a coastline.

A review of some advances in understanding oceanic boundary layers is in Ierley (1990). Mesoscale processes in the WBCs and their influence on the basin-scale circulation are still not well understood. Because of the lack of observations, not much is known about the dissipative processes in the ocean. This leaves modern theories largely unconstrained in the particular choice of subgrid-scale parameterizations of the momentum diffusion (e.g., Newtonian vs biharmonic eddy diffusion), the boundary condition (e.g., free-slip vs no-slip), and the control parameters (e.g., the eddy viscosity coefficient). Also, there is considerable uncertainty about whether the coastal regions adjacent to WBCs or the underlying bottom boundary layers provide the dominant dissipative sink in ocean gyres.

At this point numerical experimentation can help to discriminate among alternatives. For example, Blandford (1971) shows that even weak lateral momentum diffusion drastically changes the barotropic wind-driven circulation, when it is combined with no-slip boundary condition and added to bottom friction. Instead of the steady, basin-scale inertial recirculation for solutions with only bottom friction (Veronis 1966), the circulation develops a separated, meandering eastward jet and transient disturbances near the western boundary, as in the case with lateral diffusion alone (Bryan 1963).

Corresponding author address: Dr. Pavel S. Berloff, Institute of Geophysics and Planetary Physics, University of California, Los Angeles, Los Angeles, CA 90095-1567.
E-mail: pavel@atmos.ucla.edu

In a model of the Somali Current, Cox (1979) finds that the current contains a sequence of propagating transient eddies. In an attempt to explain this phenomenon and the disturbances seen by Bryan (1963), Ierley and Young (1991, hereafter IY) consider the viscous instability of a barotropic WBC. They model the WBC as a parallel flow in an unbounded, barotropic north–south channel. Ierley and Young show that the flow becomes unstable at moderate values of Re; the most unstable eigenmodes are trapped near the western boundary; and the eigenmodes that are not trapped (the channel modes) become unstable only at substantially larger values of Re.

Another example of an active WBC is the East Australian Current, which is filled with mesoscale eddies (e.g., Feron 1995). Cessi and Ierley (1993) extended the results of IY and looked at linear stability and weakly nonlinear dynamics of a barotropic WBC in a channel tilted at an angle with respect to the north–south direction. They show that the negative tilt, as for the East Australian Current, favors instability of the flow.

The wind-driven, time-dependent gyre circulation's dependence on the lateral boundary condition is explored by Haidvogel et al. (1992). It is shown that in the no-slip limit the time-mean circulation develops two distinct eastward jets. In the free-slip limit both time-mean jets merge in a single jet deeply penetrating into the interior of the basin. In the latter case, the energy is much larger, and bottom friction dominates over lateral friction as the energy dissipator. Thus, changes of the lateral boundary condition lead to significant changes in the WBC dynamics that, in turn, influence the basin-scale circulation.

The eigenmodes associated with the WBC disturbances of the steady single-gyre circulation are explored in the barotropic (Sheremet et al. 1997) and the 2-layer baroclinic models (Berloff and Meacham 1998b). It is shown that the disturbances belong to a particular type of local instability, and the other types are instabilities of the recirculation gyre, standing meander, basin modes, resonant mode, and complex patterns involving several recirculations.

b. Statement of the problem

We focus on the WBC with a prescribed mean density stratification and no thermohaline forcing. This allows us, for simplicity, to use the quasigeostrophic (QG) approximation. The approximation excludes large excursions of isopycnal surfaces. In particular, it excludes outcropping, that is, intersections of the isopycnal surfaces and the bottom or upper surface. For simplicity we choose the western boundary to be straight and directed from north to south. To make orderly progress, we defer for now any consideration of sloping bottom topography near the western boundary. As the frictional operator, we use only lateral Newtonian eddy diffusion. We consider both no-slip and free-slip boundary conditions.

Within the model we address the following questions:

1) What are the critical Reynolds numbers, Re_{cr}, and the most unstable patterns associated with linear instability of the steady boundary current?
2) What are the equilibrium dynamical regimes of the time-dependent, nonlinear WBC at intermediate and large Re?
3) How does the WBC dynamics depend upon control parameters of the problem?
4) What are global patterns associated with local instabilities in the WBC?

c. The model

We model the wind-driven circulation by the quasigeostrophic equations (Holland 1978). For M active layers (we use $M = 3$), the equations for $i = 1, M$ are

$$\frac{\partial \zeta_i}{\partial t} + J(\psi_i, \zeta_i) + \beta \frac{\partial \psi_i}{\partial x} = \frac{\delta_{i,1}}{\rho_1 H_1} \nabla \times \tau + \nu \nabla^4 \psi_i, \quad (1)$$

where $\delta_{i,j} = 1$ if $i = j$ and $\delta_{i,j} = 0$ if $i \neq j$, and i is the layer index starting from the top. In (1), $\nabla \times \tau$ is the wind stress curl acting in the upper layer; ν is the eddy viscosity coefficient; and $\beta = 2 \times 10^{-11}$ m^{-1} s^{-1} is the planetary vorticity gradient. The ocean depth is $H = 4000$ m. For $M = 3$ the layer depths are usually chosen as $H_1 = 300$ m, $H_2 = 700$ m, and $H_3 = 3000$ m, except in section 3h, where H_i is varied. The wind stress is chosen to be symmetric about the middle ($y = 0$) of the basin,

$$\tau(y) = \tau_0 \cos\left(\frac{2\pi y}{L}\right),$$

where $-L/2 \leq y \leq L/2$. The streamfunction ψ_i is obtained from the elliptic problem,

$$\nabla^2 \psi_i - (1 - \delta_{i,1}) S_{i,1} (\psi_i - \psi_{i-1}) - (1 - \delta_{i,M}) S_{i,2} (\psi_i - \psi_{i+1}) = \zeta_i, \quad (2a)$$

where

$$S_{i,1} = f_0^2 \left(H_i g \frac{\rho_i - \rho_{i-1}}{\rho_1} \right)^{-1}$$

$$S_{i,2} = f_0^2 \left(H_i g \frac{\rho_{i+1} - \rho_i}{\rho_1} \right)^{-1} \quad (2b)$$

are the stratification factors with Coriolis frequency $f_0 = 0.83 \times 10^{-4}$ s^{-1}. The lateral boundary conditions are of no normal flow,

$$\psi_{i|C} = \Gamma_i(t), \quad (3)$$

and either no-slip,

$$\left.\frac{\partial \psi_i}{\partial n}\right|_C = 0, \tag{4a}$$

or free-slip,

$$\left.\frac{\partial^2 \psi_i}{\partial n^2}\right|_C = 0, \tag{4b}$$

where n is a local coordinate oriented perpendicular to the lateral boundary. This is supplemented by the integral mass conservation constraint for each layer:

$$\frac{\partial}{\partial t}\iint_A \psi_i(x, y)\, dx\, dy = 0. \tag{5}$$

Here C is the bounding contour of the domain with area A.

Our numerical model is similar to that used by Holland (1978). We have two different spatial domains: a full basin that is a square with solid boundaries all around and a north–south periodic channel with solid boundaries on its east and west sides. The dimensional (SI units) equations (1) are discretized on a uniform grid with second-order finite differences and are solved numerically using the boundary conditions (3) and either (4a) or (4b) with the mass constraint (5). The elliptic problem (2) is solved by a direct solver in the full basin and by a multigrid solver (because of the periodic boundary conditions) in the periodic channel. The grid size is chosen to be fine enough to adequately resolve the viscous western boundary layer scale,

$$\delta_M = \left(\frac{\nu}{\beta}\right)^{1/3}. \tag{6}$$

We find empirically that for our range of parameters the minimum resolution is about two grid intervals per δ_M.

2. Wind-driven gyres

Here we focus on two regimes of circulation, which are either with or without substantial instabilities in the WBCs. The latter regime was explored in the 1.5- and 2-layer approximations (Berloff and McWilliams 1999) from the large-scale, low-frequency variability point of view. It was shown that as long as the WBCs are relatively stable the variability grows with the decreasing ν. The variability is associated with structural changes of the eastward jet and adjacent recirculation zones. The main difference here is that we use a 3-layer approximation in order to destabilize the WBC at larger values of ν.

We choose a basin dimension of $L = 3840$ km and a wind stress amplitude of $\tau_0 = 0.03$ N m^{-2}. The density jumps, $\Delta\rho_i = \rho_{i+1} - \rho_i$, are such that the first baroclinic deformation radius Rd_1 (appendix B) is 52 km. We experiment with different values of ν and both types of the boundary condition (4).

With $\nu = 1500$ m^2 s^{-1}, the flow with the no-slip boundary condition is stable and confined to the upper layer in the large-time limit. The circulation has the pattern of two gyres, subtropical and subpolar, with strong WBCs that separate at the middle latitude, $y = 0$, and turn eastward with a narrow width of about 100 km. At $\nu = 1000$ m^2 s^{-1}, in the large-time limit, the solution converges to a limit cycle with a small amplitude of 0.02% of the total energy. The total energy is defined as the basin integral of the energy density

$$E(x, y, t) = \frac{1}{A}\sum_{i=1,3}\frac{H_i}{H}\frac{|\nabla\psi_i|^2}{2} + \frac{S_{1,2}H_1 + S_{2,1}H_2}{4(H_1 + H_2)A}(\psi_1 - \psi_2)^2 + \frac{S_{2,2}H_2 + S_{3,1}H_3}{4(H_2 + H_3)A}(\psi_2 - \psi_3)^2. \tag{7}$$

The motion on the limit cycle is characterized by the presence of transient vortices in the WBC. The vortices propagate along the boundary toward the middle latitude. Thus, the primary Hopf bifurcation of the flow originates due to local instability of the WBC.

In order to see changes of the flow associated with a further decrease of ν, we examine another no-slip solution at $\nu = 500$ m^2 s^{-1} (with a spatial grid size of 15 km). An instantaneous picture of the solution is shown in Figs. 1a–c. The circulation contains well-defined mesoscale eddies in the WBCs and in the adjacent portions of the westward flanks of the gyres. The basin-averaged total energy time series, part of which is shown in Fig. 2a, indicates that the relative amplitude of the fluctuations around the time-mean energy is about 0.8%. The power spectrum of the time series is shown in Fig. 2b. To quantify the amount of the low-frequency variability present in the solution, we split the spectrum into three frequency bands: the mesoscale band (M) with frequencies larger than 1.74 yr^{-1} (periods less than 210 days); the quasiannual band (Q) with frequencies between 0.58 and 1.74 yr^{-1} (periods between 210 and 630 days); and the interannual (I) band with frequencies less than 0.58 yr^{-1} (periods longer than 630 days). The spectrum contains about 70% of the power in the interannual band, consistent with the results of Berloff and McWilliams (1999). The most interesting feature of the flow is the absence of a single, intense eastward jet. Instead, the eastward flow is very broad and intensified on its southern and northern edges. The distance between the edges of the eastward flow is about 1000 km. A similar double-jet structure of the eastward flow was found by Haidvogel et al. (1992) in the no-slip case.

The eddies, which start to form in the westward flanks of the gyres, grow in amplitude as they propagate downstream. About 600 km away from the middle latitude, the eddies become strong enough to separate the flow from the wall. This behavior is illustrated by the separation diagram shown in Fig. 3. The solution yields the energy conversion (17a,b) that is predominantly baro-

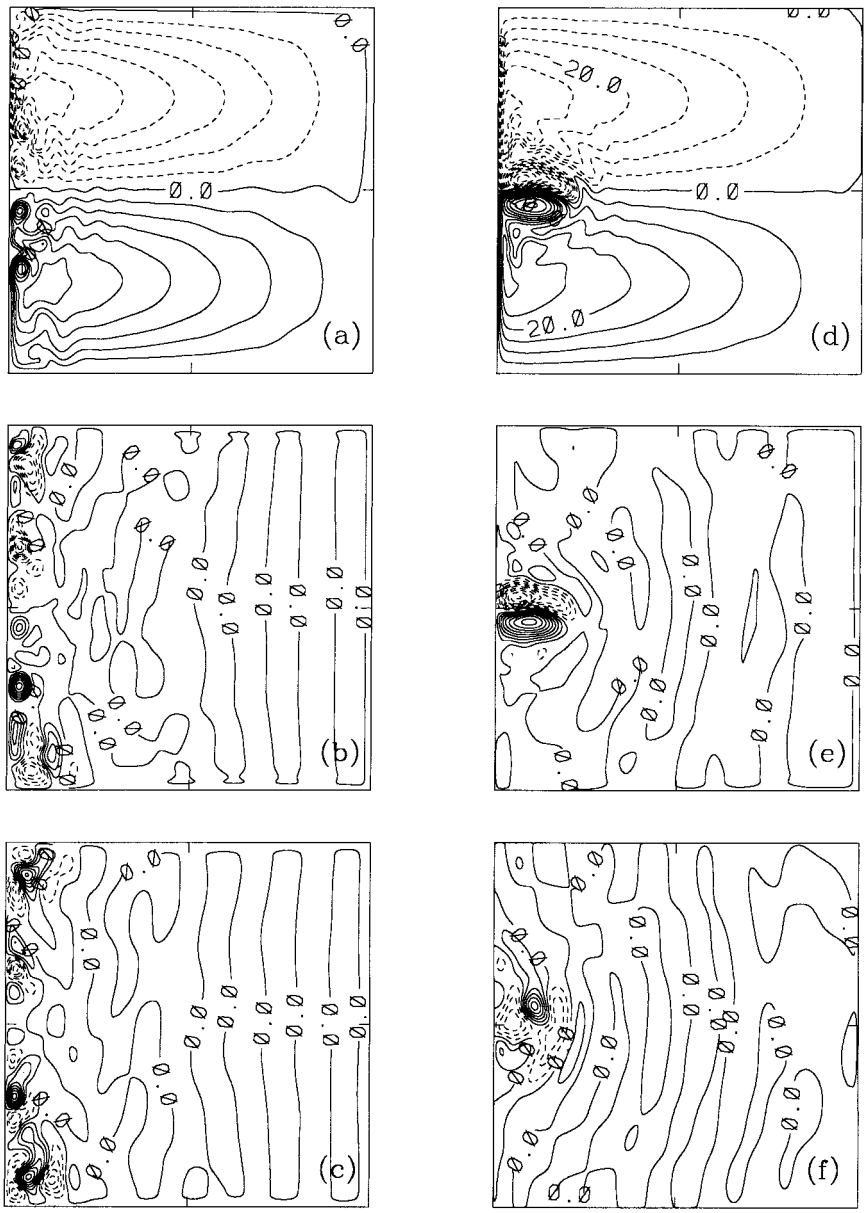

FIG. 1. Snapshots in all three layers for a basin solution with $\nu = 500$ m^2 s^{-1}. The no-slip case: (a) ψ_1, (b) ψ_2, (c) ψ_3. The free-slip case: (d) ψ_1, (e) ψ_2, (f) ψ_3. CI $= 5 \times 10^3$ in (a) and (d); CI $= 2 \times 10^3$ in (b) and (e); CI $= 5 \times 10^3$ in (c) and (f).

clinic in the WBCs. This is consistent with the linear and finite amplitude results of the local model (sections 3 and 4).

As an example of the flow without eddy generation in the WBCs, in Figs. 1d–f we show snapshots of a free-slip circulation with the same parameters as in the no-slip counterpart. The flow has the familiar pattern of a pair of surface intensified recirculation cells (Holland 1978). Berloff and McWilliams (1999) study the low-frequency variability in this regime and show that the dipole recirculation pattern is an attribute of the double gyre with the wind stress close to symmetrical. The basin-averaged total energy time series of the free-slip circulation is shown in Fig. 2c. The time series contains fluctuations with a relative amplitude about 26%. This is substantially larger than the relative amplitude of the no-slip circulation. The time series power spectrum (Fig. 2d) contains more than 96% of the spectral power within the interannual band, a substantial amount. Comparison with the no-slip solution suggests that the low-frequency variability increases when the boundary condition is free slip. The stabilizing effect of the free-slip boundary on the WBC dynamics is explored in sections 3g and 4d in the local channel model. Here, we only illustrate that

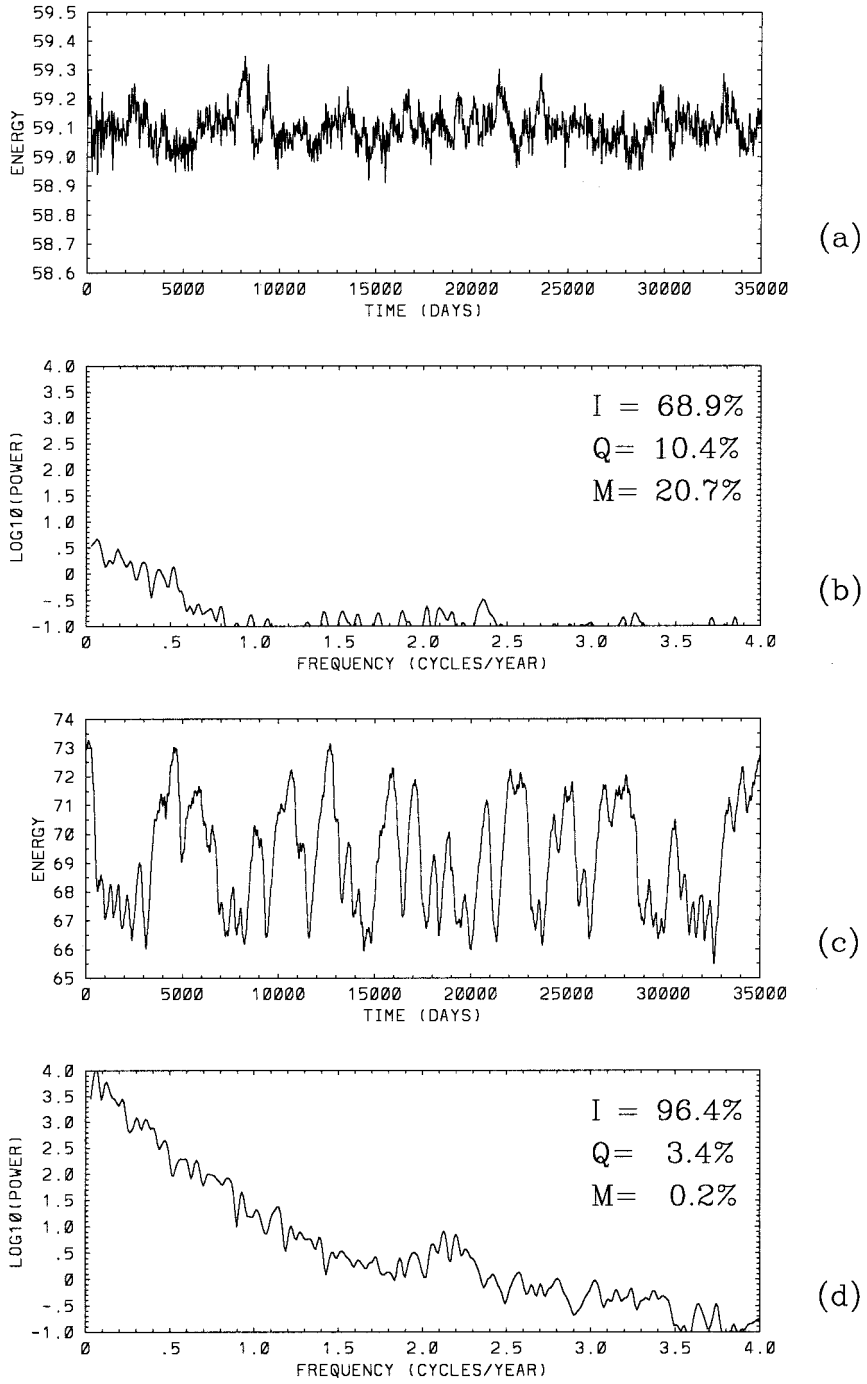

FIG. 2. Time series and spectra of the basin-averaged total energy for a basin solution with $\nu = 500$ m^2 s^{-1} and either (a, b) no-slip or (c, d) free-slip boundary condition; I, Q, and M denote the relative power in the interannual, quasiannual, and mesoscale frequency bands, respectively.

the WBC instability correlates with global changes of the circulation such as the absence of a single narrow eastward jet, the appearance of the recirculation dipole, and the substantial drop in the low-frequency variability. Still it is not clear to what extent the WBC instabilities and transient eddies are responsible for the global changes of the gyre circulation.

How robust is the no-slip double-gyre dynamics with respect to variations of the control parameters? We made a modest survey in alternative values of the viscosity coefficient ($100 < \nu < 1500$ m^2 s^{-1}), the stratification profile [$1 < (\rho_2 - \rho_1)/(\rho_3 - \rho_2) < 2$; $40 < \mathrm{Rd}_1 < 52$ km], and the pattern of the wind stress ($0 < \lambda < 2$; $0.03 < \tau_0 < 0.04$ N m^{-2}). In all the cases we found

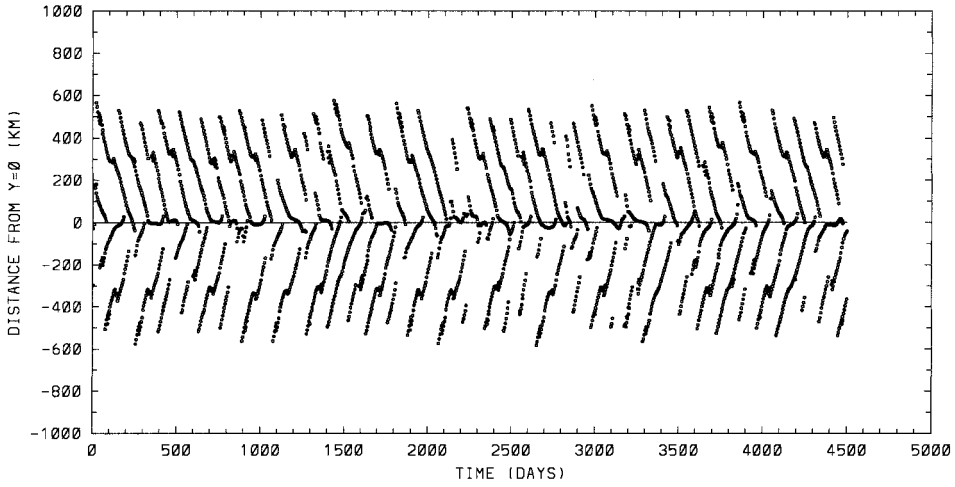

FIG. 3. A scatter diagram of boundary-current separation points at different times for the no-slip basin solution with $\nu = 500$ m^2 s^{-1}.

that the WBCs are unstable and there are eddies and meanders generated inside them. This suggests, in accordance with the earlier work of Haidvogel et al. (1992), that the significant WBC instability is a robust phenomenon when ν has sufficiently small values and when there is no-slip lateral condition on the western boundary. We emphasize that this conclusion is drawn in the absence of sloping topography near the western boundary, tilting of the western boundary with respect to the north–south direction, and outcropping of the isopycnal surfaces. The influences of all these aspects on the baroclinic wind-driven gyres at even moderate values of Re have not been fully explored.

3. Linear stability of the WBC

a. Linearized model

We model the steady WBC as a flow parallel to the western wall in a north–south periodic channel on the β plane. The steady state is motionless in the second and third layers and it has the Munk (1950) velocity profile in the upper layer. For the reason of dynamical complexity, we defer considering non-parallel steady states, and the states with non-zero flow in the deep layers. In the no-slip situation the upper layer velocity is

$$\overline{v}_1 = V_0 \exp\left(-\frac{x}{2\delta_M}\right) \sin\left(\frac{\sqrt{3}x}{2\delta_M}\right). \tag{8a}$$

This velocity profile has its maximum away from the wall. In the free-slip case the steady flow is

$$\overline{v}_1 = V_0 \frac{\sqrt{3}}{2} \exp\left(-\frac{x}{2\delta_M}\right)\left[\cos\left(\frac{\sqrt{3}x}{2\delta_M}\right) + \frac{1}{\sqrt{3}} \sin\left(\frac{\sqrt{3}x}{2\delta_M}\right)\right]. \tag{8b}$$

The velocity has its maximum at $x = 0$. The normalization factor $\sqrt{3}/2$ makes the total transport, $W_1 = H_1 \int_0^{+\infty} v_1\, dx$, to be the same for the same V_0 in both cases.

We are interested in determining the critical values of the Reynolds number,

$$\mathrm{Re} = \frac{V_0 \delta_M}{\nu} = \frac{\psi_0}{\nu}, \tag{9}$$

when the steady WBC is only marginally stable. Given Re, the total transport of the steady state is

$$W_1 = \frac{\sqrt{3}}{2} H_1 V_0 \delta_M = \frac{\sqrt{3}}{2} H_1 \nu \mathrm{Re}. \tag{10}$$

The governing equations for the perturbation streamfunctions ψ_i $(i = 1, 3)$ are obtained by linearizing around the steady state and they are

$$\begin{aligned}
&\frac{\partial}{\partial t}[\nabla^2\psi_1 - S_{1,2}(\psi_1 - \psi_2)] + \overline{v}_1 \frac{\partial}{\partial y}(\nabla^2\psi_1 + S_{1,2}\psi_2) \\
&\quad - \overline{v}_{1xx} \frac{\partial \psi_1}{\partial y} + \beta \frac{\partial \psi_1}{\partial x} = \nu \nabla^4 \psi_1 \\
&\frac{\partial}{\partial t}[\nabla^2\psi_2 - S_{2,1}(\psi_2 - \psi_1) - S_{2,2}(\psi_2 - \psi_3)] \\
&\quad - S_{2,1}\overline{v}_1 \frac{\partial \psi_2}{\partial y} + \beta \frac{\partial \psi_2}{\partial x} = \nu \nabla^4 \psi_2 \\
&\frac{\partial}{\partial t}[\nabla^2\psi_3 + S_{3,1}(\psi_2 - \psi_3)] + \beta \frac{\partial \psi_3}{\partial x} = \nu \nabla^4 \psi_3,
\end{aligned} \tag{11}$$

where $S_{1,2}$, $S_{2,1}$, $S_{2,2}$, $S_{3,1}$ are defined in (2b).

b. Eigenvalue problem

We look for normal mode solutions of (11) in the form

$$\psi_i(x, y, t) = e^{i(\alpha y - \omega t)} \tilde{\psi}_i(x) + e^{-i(\alpha y - \omega t)} \tilde{\psi}_i^*(x), \tag{12}$$

TABLE 1. Critical no-slip eigenmode values for fixed ν.

ν ($m^2\ s^{-1}$)	V_{max} ($m\ s^{-1}$)	α_{cr} (δ_M^{-1})	l_y (km)	ω_{cr} ($Re_{cr}\nu\delta_M^{-2}$)	T (days)	c_g (km day^{-1})
2000	0.24	0.58	500	0.043	153	3.7
1000	0.20	0.55	420	0.047	131	3.1
500	0.18	0.49	370	0.050	114	2.5
300	0.15	0.44	350	0.053	108	2.0

where y wavelength of the mode is $l_y = 2\pi\alpha^{-1}$ and the time period is $T = 2\pi\mathrm{Re}(\omega)^{-1}$. The normal mode decomposition of (11) yields the following system of equations for $\tilde{\psi}_i$:

$$\tilde{\psi}_1^{\mathrm{IV}} - \left(2\alpha^2 + i\frac{\alpha}{\nu}\overline{v}_1\right)\tilde{\psi}_1'' - \beta\tilde{\psi}_1' + \left(\alpha^4 + i\frac{\alpha^3}{\nu}\overline{v}_1 + i\frac{\alpha}{\nu}\overline{v}_{1xx}\right)\tilde{\psi}_1 - i\frac{\alpha}{\nu}S_{1,2}\overline{v}_1\tilde{\psi}_2 = i\frac{\omega}{\nu}[-\tilde{\psi}_1'' + (\alpha^2 + S_{1,2})\tilde{\psi}_1 - S_{1,2}\tilde{\psi}_2]$$

$$\tilde{\psi}_2^{\mathrm{IV}} - 2\alpha^2\tilde{\psi}_2'' - \beta\tilde{\psi}_2' + \left(\alpha^4 + i\frac{\alpha}{\nu}S_{2,1}\overline{v}_1\right)\tilde{\psi}_2 = i\frac{\omega}{\nu}[-\tilde{\psi}_2'' + (\alpha^2 + S_{2,1} + S_{2,2})\tilde{\psi}_2 - S_{2,1}\tilde{\psi}_1 - S_{2,2}\tilde{\psi}_3]$$

$$\tilde{\psi}_3^{\mathrm{IV}} - 2\alpha^2\tilde{\psi}_3'' - \beta\tilde{\psi}_3' + \alpha^4\tilde{\psi}_3 = i\frac{\omega}{\nu}[-\tilde{\psi}_3'' + (\alpha^2 + S_{3,1})\tilde{\psi}_3 - S_{3,1}\tilde{\psi}_2]. \quad (13)$$

The width of the channel is a parameter of the problem, but we are interested in the situation where the eastern wall has no significant influence on the dynamics. Ierley and Young show that the eastern wall has no influence on the linearized barotropic WBC if the channel width is much larger than the x scale of the trapped eigenmodes. Therefore, we fix the channel width at $L_x = 30\delta_M$. This is a large scale in comparison with the trapped marginal eigenmode. The boundary conditions at $x = 0$, L_x are

$$\tilde{\psi}_i(0) = \tilde{\psi}_i(L_x) = 0, \quad (14)$$

and, in the case of no-slip, also

$$\tilde{\psi}_i'(0) = \tilde{\psi}_i'(L_x) = 0, \quad (15a)$$

or, in the case of free-slip,

$$\tilde{\psi}_i''(0) = \tilde{\psi}_i''(L_x) = 0. \quad (15b)$$

The layer depths and densities are given in section 2, except when explicitly varied (section 3h) in order to explore dependence of the solution upon them. The eigenvalue problem (13), (14), and (15) is solved numerically, with 100 points in x for the finite difference discretization, except for appendixes A and B, where the resolution is up to 500 points when it is necessary to resolve the boundary layer scales. An increase in resolution from 100 to 120 points yields changes in Re_{cr} that are less than 1%. This indicates that 100 points give a reliable result.

c. Marginal stability as a function of ν

The stability of the flow at asymptotically large values of ν is analyzed in appendix A. The main conclusion from the analysis in appendix A is that all the eigenmodes are stable viscous channel modes with the viscous length scale $[L] = \delta_M \sim \nu^{1/3}$, and the timescale $[T] = \delta_M\beta^{-1}\mathrm{Rd}_1^{-2} \sim \nu^{1/3}$, of the long baroclinic Rossby wave. The main balance (A6) is between the stretching term, advection of the planetary vorticity, and friction. All eigenmodes are stable, and the least stable eigenmodes correspond to $\alpha \to 0$.

At intermediate values of ν, the problem is explored by varying V_0, hence by varying Re, while keeping four values of ν: 2000, 1000, 500, and 300 $m^2\ s^{-1}$ fixed. The boundary condition is no-slip, and $\mathrm{Rd}_1 = 52$ km. The values of maximum velocity V_{max}, α_{cr}, l_y, $\mathrm{Re}(\omega_{cr})$, T, and the group velocity c_g of the critical eigenmode are summarized in Table 1.

Both the y wavelength, l_y, and the time period, T, decrease with ν, and their typical values are several hundred kilometers and several months.

The marginal stability curves (W_1, α) and $[W_1, \mathrm{Re}(\omega)]$ are shown in Figs. 4a,b. The critical transport value, W_{1cr}, corresponds to the ''nose'' of each curve. It gradually decreases with decreasing ν. However, the dependence of W_{1cr} on ν is not linear as might be expected from (10) because, as our results show, Re_{cr} approximately depends on ν as

$$\mathrm{Re}_{cr} \sim \nu^{-0.4}. \quad (16)$$

Why does Re_{cr} increase with decreasing ν, in the range of the variations? To answer this question the barotropic and baroclinic energy conversions (Pedlosky 1987) between the steady state and the critical eigenmode are calculated. In section 4 we use the same approach to calculate the energy conversions between the time-mean states and the finite amplitude perturbations.

For the 3-layer stratification and parallel north–south background flow, the barotropic energy conversion integrand is

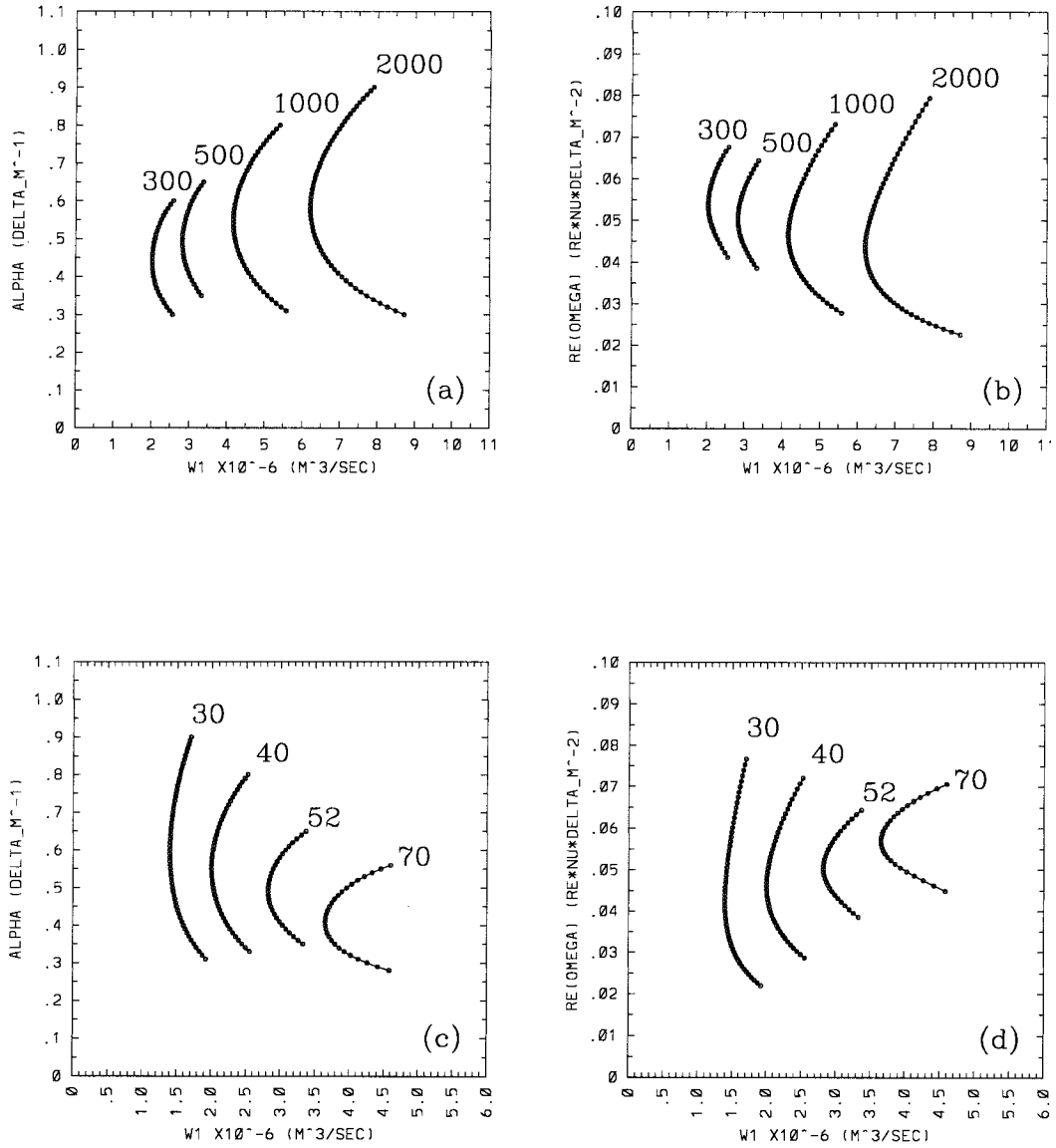

FIG. 4. Marginal stability curves (W_1, α) and [W_1, Re(ω)] for no-slip condition. (a, b) Rd_1 = 52 km (ν = 2000, 1000, 500, and 300 m^2 s^{-1}). In the limit $\nu \to 0$ (see appendix A): $\alpha \to 0.33\delta_M^{-1}$ and Re(ω) $\to 0.079$Re $\nu\delta_M^{-2}$. (c, d) ν = 500 m^2 s^{-1} (Rd_1 = 30, 40, 52, and 70 km).

$$\mathrm{BT}(x) = \sum_{i=1,3} \frac{H_i}{H}\langle \psi'_{ix}\psi'_{iy}\Psi_{ixx}\rangle, \tag{17a}$$

and the baroclinic energy conversion integrand is

$$\mathrm{BCL}(x) = \frac{S_{1,2}S_{2,1}}{S_{1,2}+S_{2,1}}\left\langle(\psi_1-\psi_2)\frac{1}{2}(\psi_1+\psi_2)_y(\Psi_1-\Psi_2)_x\right\rangle \times \frac{S_{2,2}S_{3,1}}{S_{2,2}+S_{3,1}}\left\langle(\psi_2-\psi_3)\frac{1}{2}(\psi_2+\psi_3)_y(\Psi_2-\Psi_3)_x\right\rangle, \tag{17b}$$

where H is the total fluid depth and $\langle\cdot\rangle$ denotes a (y, t) average. When the x integral of the total conversion is positive, perturbations gain energy from the basic flow. In the range of the parameters explored, we find that BCL strongly dominates for the critical eigenmode; thus, the primary instability is essentially baroclinic. From the simple scaling arguments in appendix A, it follows that the barotropic conversion dominates for sufficiently small values of ν. On the other hand for sufficiently small ν there is a continuum of very unstable eigenmodes. Therefore, it is likely that the finite amplitude dynamics of the statistically stationary flow is turbulent, and the linear approach is of little value.

The predominantly baroclinic instability reported here is different from the purely barotropic instability considered by IY. It also is different from the instability

TABLE 2. As in Table 1 but for fixed Rd_1.

Rd_1 (km)	V_{max} (m s^{-1})	a_{cr} (δ_M^{-1})	l_y (km)	ω_{cr} ($Re_{cr}\nu\delta_M^{-2}$)	T (days)	c_g (km day^{-1})
70	0.23	0.41	450	0.057	77	3.3
52	0.18	0.49	370	0.050	114	2.5
40	0.13	0.55	330	0.046	175	1.9
30	0.09	0.59	310	0.043	270	1.9

of an east–west baroclinic jet, where the two conversion amplitudes are usually similar (Haidvogel and Holland 1978). Ikeda (1983) shows a stabilization of barotropic instability due to the side boundary in a baroclinic model of a zonal current. To some extent the same result can hold for the western wall of the WBC, which further adds to the baroclinic instability dominance. At higher Re, as suggested by (A5), the contribution of the barotropic energy conversion grows.

In general, broad currents with width larger than Rd_1 are more subject to baroclinic rather than barotropic instability (Pedlosky 1987). In our situation, larger ν correspond to broader currents, that are more susceptible to baroclinic instability, and therefore have smaller Re_{cr}. Apart from this qualitative explanation, we cannot explain the empirical relationship (16). On the other hand, this relationship is transitional and would not persist with an indefinite decrease in ν.

Why does α decrease and $\mathrm{Re}(\omega)$ increase with decreasing ν? In appendix A, we show that in the limit $\nu \to 0$ the characteristic length scale of perturbation is $[L] = \delta_M \sim \nu^{1/3}$, and the timescale is advective: $[T] = \delta_M^2\psi_0^{-1} \sim \nu^{2/3}$. The eigenmodes are well trapped near the western boundary and are confined to the upper layer. In the no-slip situation there is the viscous sublayer that scales as $[L] = \delta_M \mathrm{Re}^{-1/2} \sim \nu^{5/6}$. In the limit $\nu \to 0$, the most unstable y wavenumber approaches $\alpha = 0.33\delta_M^{-1}$, and the corresponding eigenfrequency approaches $\mathrm{Re}(\omega) = 0.079\mathrm{Re}\nu\delta_M^{-2}$. This is consistent with the tendencies explored in this paragraph and illustrated in Figs. 4a and 4b.

d. Marginal stability as a function of Rd_1

The stability of the current strongly depends on Rd_1. In Figs. 4c and 4d we show the marginal stability curves for $\nu = 500$ m^2 s^{-1} and four values of Rd_1: 30, 40, 52, and 70 km. The values of maximum velocity V_{max}, α_{cr}, l_y, $\mathrm{Re}(\omega_{cr})$, T, and c_g of the critical eigenmodes are summarized in Table 2.

In our range of Rd_1 variation, if Rd_1 decreases, the critical transport decreases substantially,

$$\mathrm{Re}_{cr} \sim \mathrm{Rd}_1^{1.2}, \tag{18}$$

the critical y wavelength decreases, and the eigenfrequency decreases with an approximate dependence:

$$\omega \sim \mathrm{Rd}_1^{1.5}. \tag{19}$$

For comparison, the frequency of long baroclinic Rossby wave scales as $\omega \sim \mathrm{Rd}_1^2$.

Qualitatively, we argue that since the instability is predominantly baroclinic, reducing Rd_1 facilitates the baroclinic instability even more and, therefore, moves the stability threshold to smaller Re_{cr} and smaller transports. This is consistent with (18), but we have no explanation of why the exponent in (18) is 1.2. A more simple question is why does l_y decrease and the period T substantially increase (Table 2) with decreasing Rd_1? In appendix B we consider (11) in the limit of small Rd_1. The limit $Rd_1 \to \infty$ corresponds to the upper-layer flow governed by the barotropic vorticity equation and to the motionless deep layers. This situation is considered in IY. When Rd_1 is small (see appendix B), it follows that

$$l_y \sim \mathrm{Rd}_1^{2/3}\mathrm{Re}^{-1/3}, \qquad T \sim \mathrm{Rd}_1^{2/3}\mathrm{Re}^{-4/3}.$$

Combining this scaling with the empirical relationship (18), we find that the large increase of the period and the moderate drop in l_y (see Table 2), when Rd_1 varies from 70 to 30 km, are both consistent with the predictions of the asymptotic analysis. At small Rd_1 the leading order balance is (B10); the barotropic streamfunction vanishes; and the most unstable eigenmode is confined to the first maximum of the steady state.

e. The no-slip critical eigenmode

Consider the marginal eigenmode at $\nu = 500$ m^2 s^{-1}, $Rd_1 = 52$ km, and $Re_{cr} = 21.7$. The amplitudes and phases of the corresponding $\tilde{\psi}_i(x)$ are shown in Fig. 5. The amplitudes in each layer are trapped in the western half of the channel with the upper layer maximum near $x = 2\delta_M$. The phases are mostly linear in x except for the western 20% of the channel. The phase shift between the layers is such that the perturbations are tilted against the vertical shear. This is typical (Pedlosky 1987) for the perturbations which extract energy from the mean vertical shear and transfer it down the gradient, that is, to the deep layers. The mode has $l_y = 12.8\delta_M$ (370 km) and the period $T = 114$ days (see Table 1).

At Re_{cr} and α_{cr}, the group velocity $c_g = \partial\mathrm{Re}(\omega)/\partial\alpha$ is 2.47 km day^{-1}. In bounded domains, unless c_g vanishes, the flow is *convectively* unstable, otherwise it is *absolutely* unstable (e.g., Cessi and Ierley 1993). In the former case, the disturbance will propagate with veloc-

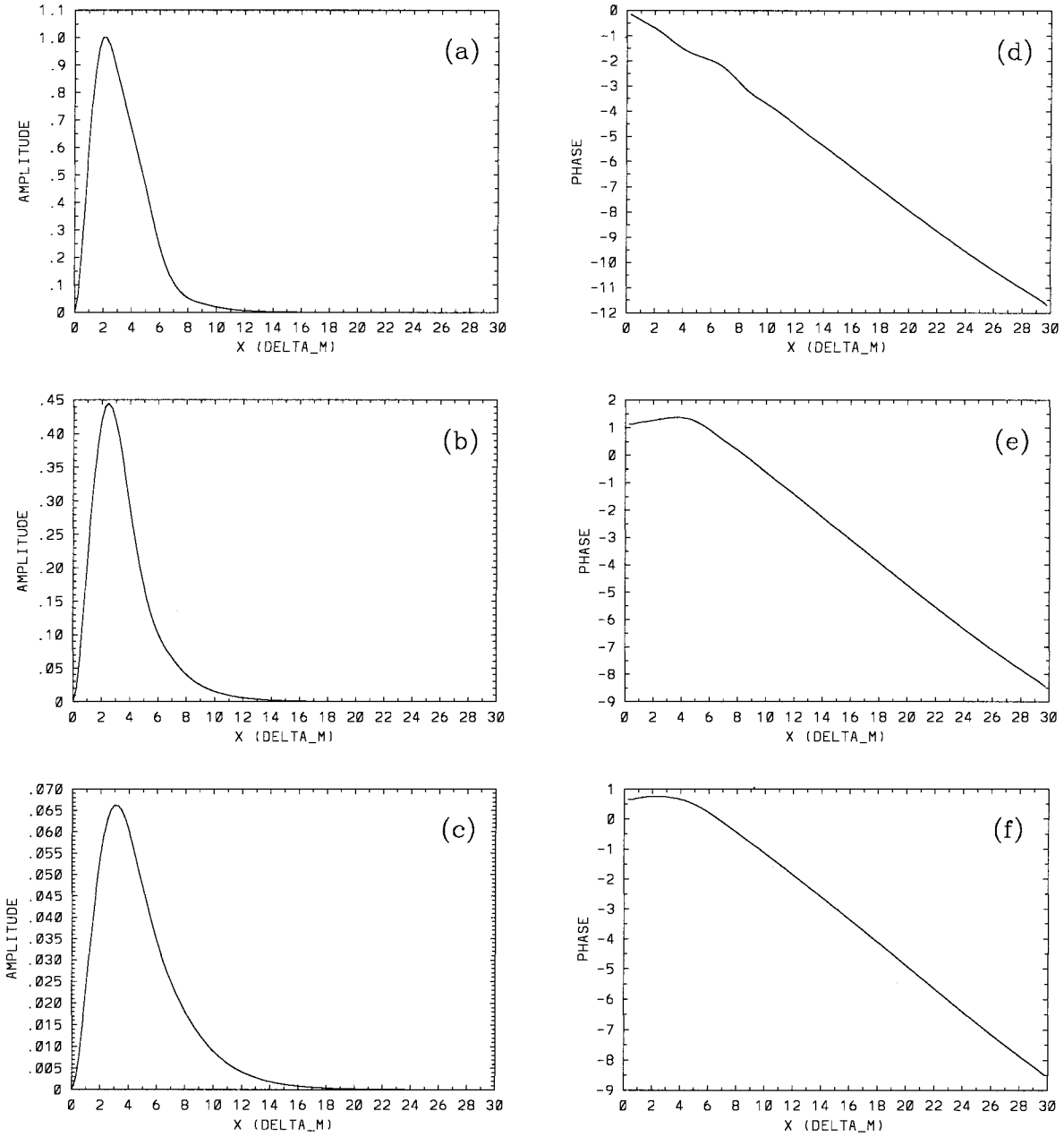

FIG. 5. The amplitude (a–c) and phase (d–f) of local critical eigenmode [(a, d) $\tilde{\psi}_1$, (b, e) $\tilde{\psi}_2$, and (c, f) $\tilde{\psi}_3$] for $\nu = 500$ m^2 s^{-1}, $\mathrm{Rd}_1 = 52$ km, and no-slip condition.

ity c_g away from the localized region of instability, and at later time it will exit the domain. In the latter case the disturbance will stay and grow in the region of instability. We find that c_g is not small. Therefore in regimes close to the linear one, the eddies generated by the instability are likely to be advected out of the western boundary and farther into the eastward jet before they gain full strength.

What happens to the most unstable (critical) eigenmode at $\mathrm{Re} > \mathrm{Re}_{\mathrm{cr}}$ if V_0 (and therefore Re) increases and other parameters are fixed at $\nu = 500$ m^2 s^{-1} and $\mathrm{Rd}_1 = 52$ km? For $\mathrm{Re} > \mathrm{Re}_{\mathrm{cr}}$, there is always a band of unstable eigenmodes with single positive growth rate maximum. The eigenmode characteristics for $\mathrm{Re}_{\mathrm{cr}} = 21.7$ ($V_0 = 0.372$ m s^{-1}) are shown in Table 1. We want to compare the critical eigenmode structure for a range of supercritical $\mathrm{Re}(V_0)$ with perturbations of the nonlinear solutions in section 4b. We find that α slowly increases with V_0 and for $V_0 = 1.7$ m s^{-1} (Re = 99): $\alpha_{\mathrm{cr}} = 0.567\delta_M^{-1}$, while Re($\omega$) remains $0.05\mathrm{Re}\nu\delta_M^{-2}$. This indicates that the timescale of the eigenmode is perfectly advective; that is, $[T] = \delta_M^2\psi_0^{-1}$, and the y wavelength

scales only approximately as δ_M and it decreases with increasing V_0.

f. Weakly damped eigenmodes

Other linear eigenmodes successively lose stability as Re increases. The second mode becomes unstable at $\mathrm{Re}_{cr} = 126$. This is a substantially larger critical value than that of the first mode. The second eigenmode is also trapped near the western wall, with the upper amplitude reaching its maximum near $x = 5\delta_M$. This is farther into the interior than in the first mode. What are the least damped modes at Re = 21.7 where the first mode is marginal (Fig. 5)? We calculated two such modes. They have negative growth rates $\mathrm{Im}(\omega) = -0.57$ and -0.94 ($\times 10^{-2}\ \psi_0\delta_M^{-2}$) and periods of 2.35 yr and about 30 yr, respectively. The modes are also trapped near the western boundary with their amplitude maxima near $x = 6\delta_M$. The second mode has $\alpha_{cr} = 0.53\delta_M^{-1}$, and the third has $\alpha_{cr} = 0.59\delta_M^{-1}$. Both values are close to α_{cr} of the first mode. This suggests that at slightly supercritical Re, the weakly damped modes may spatially resonate with the unstable one. On the other hand, as it is shown in section 4, the range of supercritical parameters, where the transient dynamics may be efficiently described in terms of the linear eigenmodes, is small. Thus, the resonance mechanism is not likely to be a general one.

What happens to the channel modes, that is, to the modes that are not completely trapped near the western wall? In all cases considered in this paper, we find that the channel modes are more stable than the trapped modes. This is consistent with the barotropic results of IY.

g. The free-slip critical eigenmode

We now compare the eigenmodes with free-slip and no-slip boundary conditions at $\nu = 500\ \mathrm{m^2\ s^{-1}}$ and $\mathrm{Rd}_1 = 52$ km. The critical transport W_{1cr} is only 4% larger in the free-slip case, suggesting that this type of boundary condition only slightly stabilizes the current. Nevertheless, the marginal eigenmode structure changes substantially. In the free-slip case: $\alpha_{cr} = 0.315\delta_M^{-1}$ is smaller by 36%; $\mathrm{Re}(\omega_{cr}) = 0.08\mathrm{Re}_{cr}\nu\delta_M^{-2}$ is larger by 60%; and $\tilde{\psi}_i(x)$ is less trapped in the west, in the lower layer it penetrates even to the eastern wall.

At Re_{cr} and α_{cr} the group velocity c_g is 6.1 km day^{-1}, which is about 2.5 times larger than that in the no-slip case. This suggests that in the near-linear situations perturbation envelopes will move away even faster than in the no-slip case. This is another important stabilizing effect of the free-slip boundary condition. Although the linear stability thresholds are similar for both the no- and free-slip boundary conditions, the no- and free-slip WBCs in the finite-amplitude gyre solutions are quite different, as it is shown in section 2. Although this may be partially due to enhanced propagation of perturbation envelopes with the free-slip condition, in section 4 we demonstrate that the most substantial differences between the no- and free-slip currents do not arise near the primary instability threshold but arise in the strongly nonlinear regimes away from it.

What happens (compare with section 3e) to the most unstable eigenmode at $\mathrm{Re} > \mathrm{Re}_{cr}$ if V_0 (and therefore Re) increases, while $\nu = 500\ \mathrm{m^2\ s^{-1}}$ and $\mathrm{Rd}_1 = 52$ km? When V_0 is increased to 0.7 m s^{-1} (Re = 41); α decreases to $0.304\delta_M^{-1}$; and $\mathrm{Re}(\omega)$ decreases to $0.073\mathrm{Re}\nu\delta_M^{-2}$. For larger V_0, both α and $\mathrm{Re}(\omega)$ remain constant indicating that $[T]$ is the advective time scale, and $[L]$ is the viscous length scale. Comparing this result with the results from section 3e, we conclude that the difference between the no- and free-slip critical eigenmodes remains large even for substantially supercritical steady states.

h. Stratification

How does the linear stability of the WBC depend upon the stratification profile? In a 3-layer model with the total depth and ρ_3 fixed, the stratification is described completely by the following parameters: $R_{1,2} = H_1/H_2$, H_3, Rd_1, and $\gamma = (\rho_2 - \rho_1)/(\rho_3 - \rho_2)$. We are interested in moderate variations around the main stratification profile ($H_1 = 300$, $H_2 = 700$, $H_3 = 3000$ m, and $\gamma = 1$) used in our study. In this case, all the terms in (11) are important. We fix $\nu = 500\ \mathrm{m^2\ s^{-1}}$, $\mathrm{Rd}_1 = 52$ km, and vary $0.1 < R_{1,2} < 1.0$ and $1 < \gamma < 3$. For each value of variable parameters we calculate $T_{cr}(R_{1,2}, \gamma)$, $\alpha_{cr}(R_{1,2}, \gamma)$, and $\mathrm{Re}_{cr}(R_{1,2}, \gamma)$ (see Fig. 6). Large values of γ and small values of $R_{1,2}$ correspond to a sharp thermocline.

The stability (i.e., Re_{cr}) substantially increases with increasing γ, and for $\gamma > 2$ it increases with decreasing $R_{1,2}$ (Fig. 6a). The y wavelength of the critical mode depends mostly on γ [see $\alpha_{cr}(R_{1,2}, \gamma)$ in Fig. 6b], and it varies from 340 ($\alpha_{cr} = 0.535\delta_M^{-1}$) to 480 km ($\alpha_{cr} = 0.385\delta_M^{-1}$). This is not a big range. The time period of the critical mode increases with decreasing both $R_{1,2}$ and γ (Fig. 6c). It is about 100 days except for small values of both $R_{1,2}$ and γ. These calculations suggest that slight sharpening of the thermocline around the main stratification profile stabilizes the flow; it increases the y scale of the instability, and it changes the time period in the direction depending on whether the sharpening was achieved by varying $R_{1,2}$ or γ. The x structure of the eigenmode does not change substantially with variations in both $R_{1,2}$ and γ.

The governing equations (11) may be simplified (appendix C) in the asymptotic limit of sharp thermocline: $\gamma \to \infty$. When $R_{1,2} \to 0$, the upper layer becomes very shallow, and it is physically rational to impose a nonzero steady flow in the middle layer. This situation is beyond the scope of this paper. For large γ, which is another way of sharpening the thermocline, the dynamics in the deep layers is that of the viscous modes (C4), and the WBC is stable. The increasing γ leads to a stabilizing effect even in the range $1 < \gamma < 3$ (Fig. 6a). For large

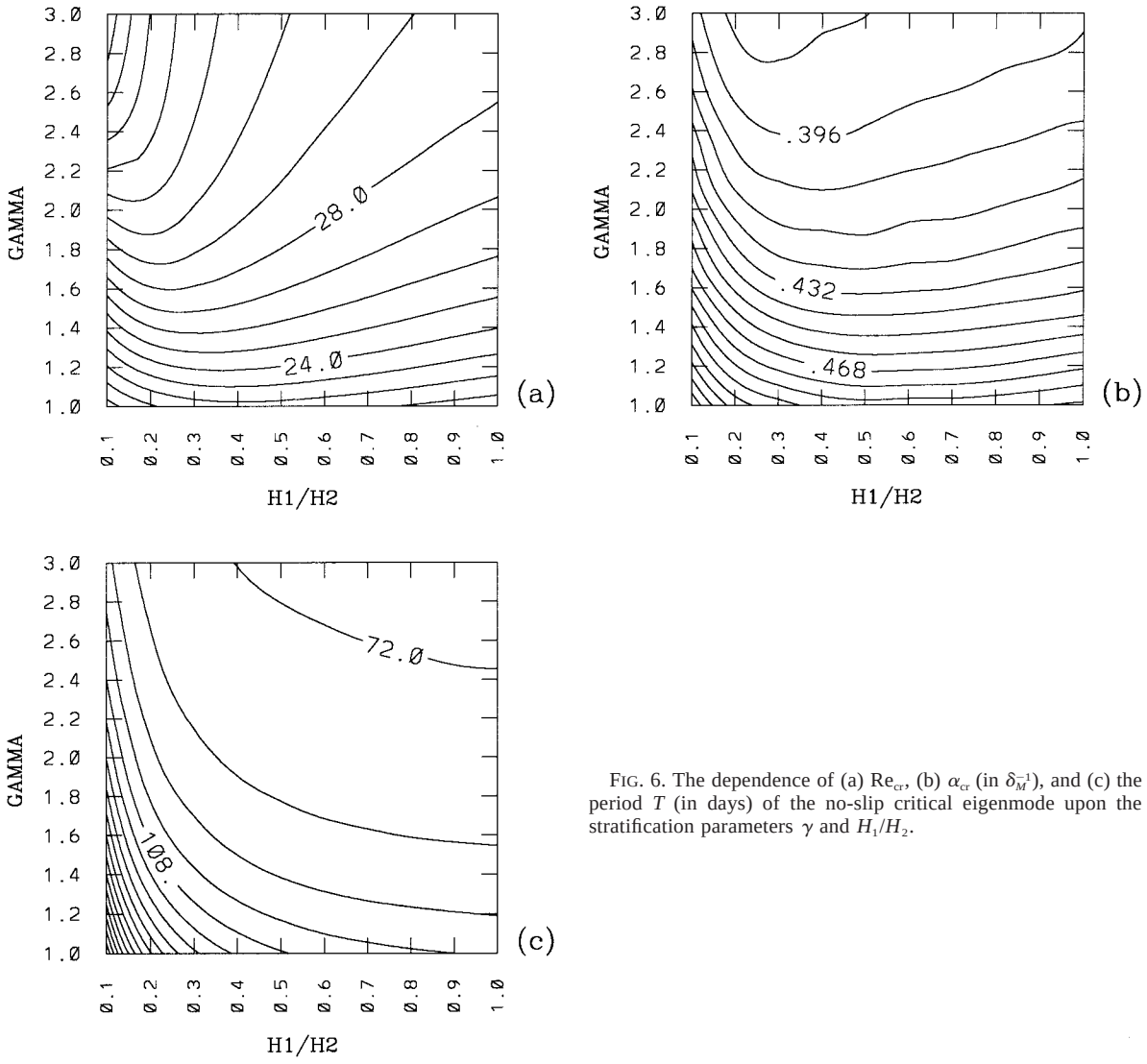

FIG. 6. The dependence of (a) Re_{cr}, (b) α_{cr} (in δ_M^{-1}), and (c) the period T (in days) of the no-slip critical eigenmode upon the stratification parameters γ and H_1/H_2.

γ, the wavenumber α of the least stable eigenmode decreases. This is consistent with Fig. 6b. In the limit $\gamma \to \infty$, the time period scales as $[T] \sim \gamma$ (appendix C). This is not observed in the range $1 < \gamma < 3$ (Fig. 6c), but for slightly larger values of γ, the period begins to increase. Also, it is shown in appendix C that the upper layer perturbation ψ_1 becomes negligible in the amplitude, relatively to $\psi_{2,3}$.

i. Comparison between the local and basin models

According to (10), the transport W_1 of the marginally stable WBC with $\nu = 500$ m^2 s^{-1} and $\mathrm{Rd}_1 = 52$ km is 2.8×10^6 m^3 s^{-1}. We compare this value to the actual boundary layer transport in the no-slip basin model from section 2. From the Sverdrup balance in the interior, we find the Sverdrup velocity $V_{\mathrm{Sv}} = \nabla \times \tau(\rho_1 H_1 \beta)^{-1}$. This yields the maximum transport across the basin: $W = 2\pi\tau_0(\rho_1\beta)^{-1} = 9.4 \times 10^6$ m^3 s^{-1}. This transport is approximately equal to the boundary current transport. Therefore, the actual transport in the basin model is about three times larger than the marginal transport in the idealized channel. This is consistent with instability of the steady WBC, hence it is consistent with the occurrence of nonlinear, time-dependent behavior.

j. Summary

Our results suggest that the WBC without sloping topography and bottom friction becomes linearly unstable at rather moderate velocity (transport). A smaller ν, shorter Rd_1, and broader stratification profile facilitate instability of the steady state. The period of the marginal mode increases with Rd_1, decreases with ν, and may change both ways for sharper thermocline. The y wavelength of the critical eigenmode decreases with Rd_1, ν,

and broader stratification profile. The eigenmode is trapped near the western boundary, and it has an oscillatory, decaying tail. The instability of the steady state occurs at similar transports in both the no- and free-slip situations. The group velocities of the eigenmodes are consistently larger in the free-slip than in the no-slip situation. Therefore the latter is more apt to be disrupted by disturbances. The instability is predominantly baroclinic in the range of explored parameters, and it occurs over the range $12 < \mathrm{Re}_{cr} < 35$ that includes the value $\mathrm{Re}_{cr} = 21.57$ found by IY in the barotropic situation.

4. Nonlinear dynamics of the WBC

a. Setup of the model

We solve for the time-dependent finite amplitude WBC in a north–south channel with x width equal to $30\delta_M$. The equations are the 3-layer QG model (section 2) without wind forcing and with periodicity in the y direction. The period L_y is a parameter of the problem. For simplicity we focus on the asymptotic limit $L_y\delta_M^{-1} \to \infty$; therefore, we choose a large value of the parameter $L_y = 240\delta_M$. We find empirically that the shorter is L_y, the less chaotic, in general, is the solution. A further step is to solve for realistic values $L_y \sim 10\delta_M$, but we defer it for the future.

Of course, we focus on small portions of the domain that are comparable with typical WBCs. The layer depths and densities are chosen as in section 2. We mostly use a slightly perturbed unstable steady state as an initial condition for time integration, except when we search for multiple equilibria. The boundary values of ψ_1, that is, the upper layer transport W_1, are fixed for all time at the steady-state values. The boundary values of $\psi_{2,3}$ are zero; therefore $W_{2,3} = 0$. On the one hand, the transports are frozen, for simplicity. On the other hand, this setup favors a more coherent response than might, otherwise, occur. A further step is to include the low-frequency variations of the transport that are consistent with those of the wind-driven gyre model, but this is beyond our present goals.

Starting with perturbed steady state, we integrate the model until it converges to a statistical equilibrium estimated from the total energy time series of a portion of the channel. The grid resolution is comparable to that of the gyre model (section 2) and it is fixed at $0.47\delta_M$.

b. Variation of the WBC strength

A sequence of solutions with $\nu = 500$ m^2 s^{-1} and with several values of V_0, that is, with different values of Re, is shown in Fig. 7. At $V_0 = 0.42$ m s^{-1}, the difference from the underlying steady state looks similar to the critical eigenmode shown in Fig. 5. This is consistent with the fact that the flow is not far from the initial bifurcation. The energy time series of this solution is chaotic; that is, it has a broadband power spectrum. The dominant spectral peak is at $T = 122$ days, which is only a bit larger than $T = 114$ days of the marginal eigenmode (section 3e). The mean distance between the eddies is $13.3\delta_M$. This is only slightly larger than $l_y = 12.8\delta_M$ of the critical eigenmode (section 3e). The chaotic behavior may be due to interaction of a few near-critical, weakly damped eigenmodes (see section 3f). At $V_0 = 0.50$ m s^{-1}, the flow becomes quasiperiodic, and its spatial structure has pronounced eddies and meanders. The two dominant periods of the quasiperiodic motion are at about 120 and 2000 days. The secondary (2000 days) mode has the y scale of the channel's period and, therefore, is likely to be distorted or even to disappear in a more realistic, gyre circulation.

At $V_0 = 0.60$ (Fig. 7b), 0.70, 0.90 (see Fig. 8), and 1.0 m s^{-1}, we find both temporally and spatially periodic solutions with the time periods of 118, 130, 133, and 131 days, respectively. The vertical structure of the periodic solution at $V_0 = 0.90$ m s^{-1} is shown in Fig. 8. The upper-layer velocity maximum is $V_{\max} = 0.40$ m s^{-1}. The flow deviates far from a parallel steady WBC by developing a sequence of intense eddies and meanders qualitatively similar to those observed in the no-slip, gyre solution in section 2. The pattern in the local model has the y period of $15.8\delta_M$ and it moves along the channel without structural changes. The perturbation is rather different from the most unstable linear eigenmode for the same value of parameters (see section 3e). The latter has the shorter y period, $12.1\delta_M$ ($\alpha = 0.52\delta_M^{-1}$), and the shorter time period, $T = 48$ days [$\mathrm{Re}(\omega) = 0.049\mathrm{Re}\nu\delta_M^{-2}$].

In comparison with the less intense WBC at $V_0 = 0.42$ m s^{-1}, we have the somewhat counterintuitive situation: the more intense is the WBC, the better it is organized, that is, there is a transition in the flow from chaotic to quasiperiodic and then to periodic. A similar situation, where an increase of the Reynolds number results in a flow with fewer degrees of freedom, is found by Berloff and Meacham (1998a) in a baroclinic, single gyre. The relative simplicity of these periodic solutions makes them an attractive target for mathematical analysis. For example, are there exact solutions of the fully nonlinear PDEs (1) and (2) in the form of the y-periodic pulse trains (Berloff and Howard 1997) in the channel?

At $V_0 = 1.1$ m s^{-1}, we again find a chaotic flow that is structurally similar to the periodic solutions. The differences are the irregular distances between the individual vortices, and the number of vortices per unit length of the channel drops approximately by a factor of 2 due to parallel flow intervals between them. When we reduce L_y to twice the width of the channel, we find that there are always two vortices per L_y and that the solution is only weakly chaotic. This shows that L_y, at moderate values, is an important control parameter. A further step, outside the scope of this paper, is to consider variations of $L_y\delta_M^{-1}$.

The turbulent nature of the WBC becomes more pronounced at $V_0 = 1.3$ and 1.7 m s^{-1} (see Fig. 7d and

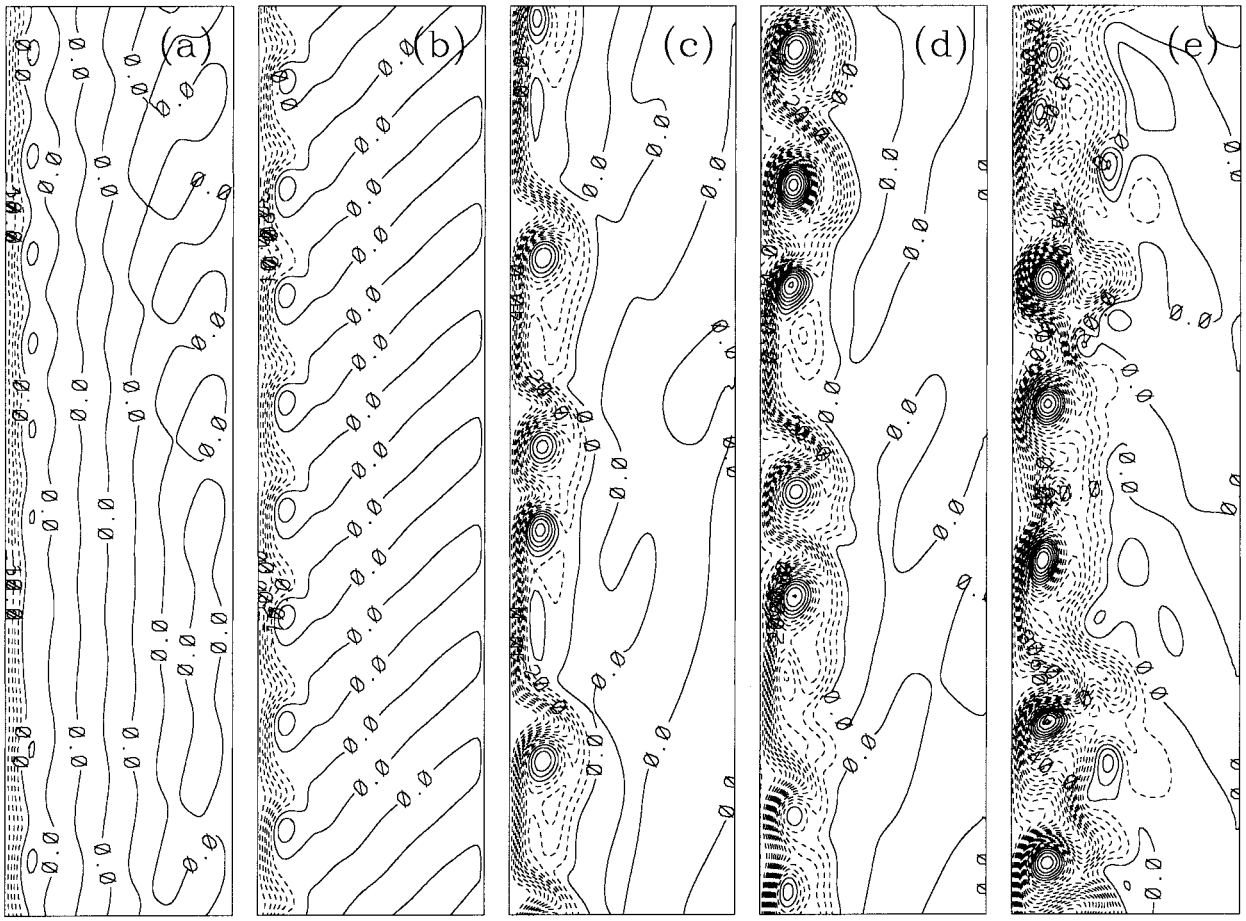

FIG. 7. Instantaneous ψ_1 for V_0 equal to (a) 0.42, (b) 0.6, (c) 1.1, (d) 1.3, and (e) 1.7 m s^{-1} (CI = 5 $\times$ 10^3). The no-slip solutions are for ν = 500 m^2 s^{-1} and Rd$_1$ = 52 km. Only one-half of the channel period is shown.

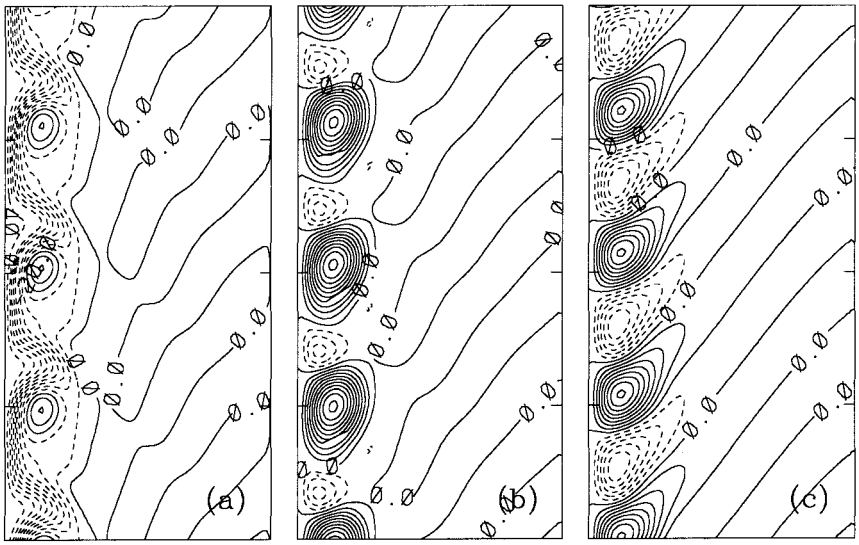

FIG. 8. The no-slip solution for ν = 500 m^2 s^{-1}, Rd$_1$ = 52 km, and V_0 = 0.9 m s^{-1}: (a) ψ_1 (CI = 5 $\times$ 10^3), (b) ψ_2 (CI = 2 $\times$ 10^3), and (c) ψ_3 (CI = 0.5 $\times$ 10^3). Only one-quarter of the channel period is shown.

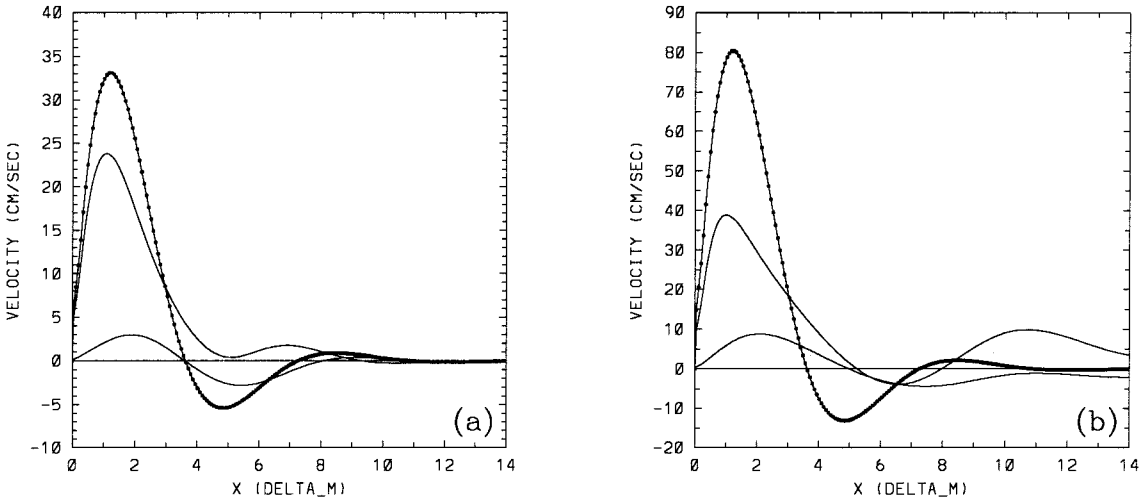

FIG. 9. Time-mean meridional velocities $\langle v_1(x)\rangle$ (large amplitude profile), $\langle v_2(x)\rangle$, and the steady-state profile (marked curve) for the no-slip solution with $\nu = 500$ m^2 s^{-1} and $\mathrm{Rd}_1 = 52$ km. (a) $V_0 = 0.7$ m s^{-1}, (b) $V_0 = 1.7$ m s^{-1}.

7e). In these cases, the number of vortices per channel period increases in comparison with the case when $V_0 = 1.1$ m s^{-1}. The meridional velocity of the time-mean flow at $V_0 = 1.7$ m s^{-1} is compared (Fig. 9b) with the underlying steady state. The time-mean upper-layer velocity decreases between the wall and, approximately, the first zero of the steady flow, and the velocity maximum shifts toward the western boundary. Also, the main counterflow shifts eastward and becomes weaker, while the second northward jet shifts in the same direction but becomes stronger. The deep layers develop the mean flows that are approximately in phase with those of the upper layer. The velocity maximum in the second layer is about 4 times smaller than that of the upper layer, and there is an even weaker flow in the third layer. Figure 9a shows that the structure of the time-mean velocities corresponding to $V_0 = 0.7$ m s^{-1} is intermediate between the stable steady state and the more turbulent current shown in Fig. 9b. We also find a solution for $V_0 = 2.5$ m s^{-1}. It is qualitatively similar to the solutions shown in Fig. 7e and Fig. 9b ($V_0 = 1.7$ m s^{-1}).

From the time-averaged potential vorticity equations, we estimate that, for all the solutions, the main balance is between the β term and the friction. (For the steady states this balance holds exactly.) The eddy flux is mostly due to the form stress, it increases with Re, and it is larger for the no-slip boundary. In the range of V_0 variations, the deeper the layer is, the larger a portion of the eddy flux the layer has in the time-mean potential vorticity balance.

The turbulent solutions contain substantial spectral power at low frequencies, but the larger is V_0, the smaller is the share of energy contained in the annual and longer time periods. We partition the spectrum into frequencies lower (LF) and higher (HF) than $\mathrm{Re}(\omega) = 1.16$ yr^{-1} (period of 314 days). Then, we compare the solutions at $V_0 = 1.1$ m s^{-1} (Fig. 7c) and at $V_0 = 1.7$ m s^{-1} (Fig. 7e). Figure 10 shows that the relative fractions of the energy in the LF band are 93% and 57%, respectively. Also, the peak near $\mathrm{Re}(\omega) = 3.5$ yr^{-1} is due to propagation of the large eddies, and it becomes more pronounced with larger V_0. The tendency of the WBC to decrease the low-frequency variability with increasing Re is opposite to the tendency observed by Berloff and McWilliams (1999) in wind-driven gyres without substantial local instabilities near the western boundary. In the latter case, the generic low-frequency variability is associated with changes in the position and shape of the eastward jet and its associated western-basin recirculation zones. Thus, we expect that moderate bursts of instability in the WBCs of the wind-driven gyres to shift the energy spectral power toward higher frequencies. The severe instabilities, as in the no-slip solution considered in section 2 or in Haidvogel et al. (1992), are correlated with the global structural changes of the eastward jet and the adjacent recirculations, which are, in turn, correlated with big changes in the low-frequency variability. Without going into the details, we observe that the low-frequency variability of each of the two eastward jets, at higher Re, is qualitatively similar to the generic variability found in Berloff and McWilliams (1999).

The energy conversions (17) are such that BCL is always much larger than BT, and it increases with V_0. From $V_0 = 0.7$ m s^{-1} to $V_0 = 1.7$ m s^{-1}, BCL increases by a factor of 7.7. The dominance of BCL conversion in the current is consistent with its dominance in the WBCs of the double-gyre solutions from section 2. From the simple scaling arguments and the linear asymptotic analysis (appendix A), it follows that for small values of ν, *BT* dominates, and the critical perturbations are intensified at the surface. This may not be true for finite-amplitude and turbulent flows. Further exploration

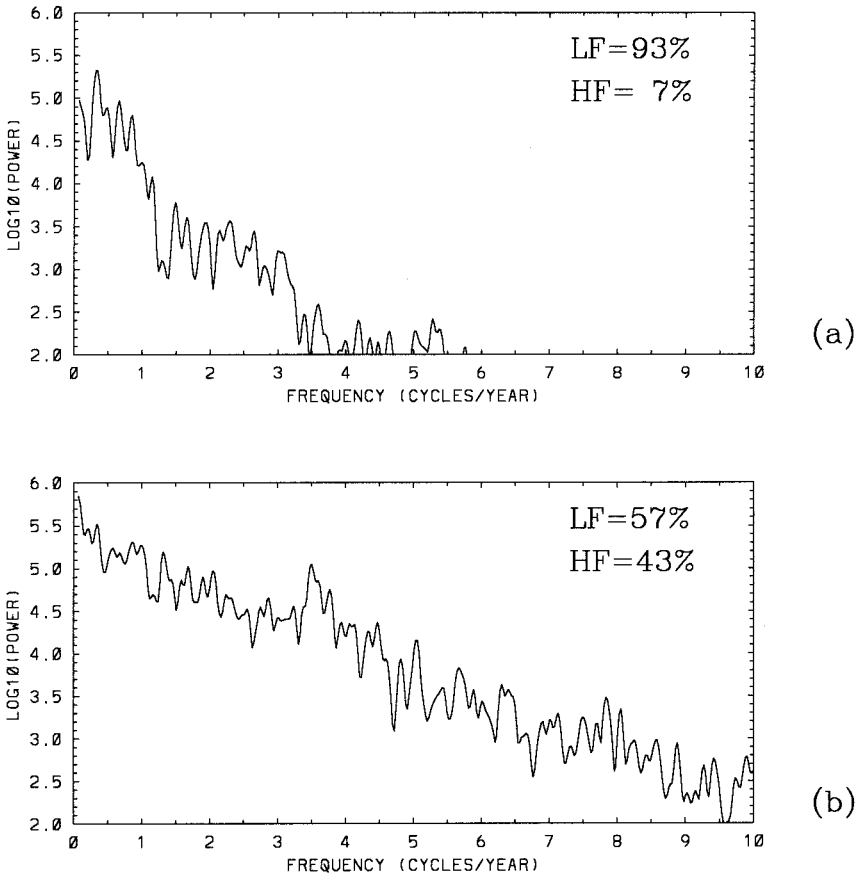

FIG. 10. Spectra of the basin-averaged total energy of no-slip solutions with $\nu = 500$ m^2 s^{-1}, $\mathrm{Rd}_1 = 52$ km; LF and HF denote the relative power in the low- and high-frequency bands, respectively. (a) $V_0 = 1.1$ m s^{-1}, (b) $V_0 = 1.7$ m s^{-1}.

is needed to understand the local model dynamics at progressively lower values of ν.

c. Variation of Rd_1

How does the dynamics depend upon Rd_1? We show a sequence of $\psi_1(x, y)$ for $\mathrm{Rd}_1 = 200$, 90, 60, and 40 km in Fig. 11. The density jumps across each interface are equal in all the cases ($\gamma = 1$), the total transport (10) corresponds to $V_0 = 1.0$ m s^{-1}, and $\nu = 500$ m^2 s^{-1}. With decreasing Rd_1, (i) the current gradually develops stronger meanders downstream from the propagating eddies, (ii) the vertical structure of the eddies is more intense in the second and third layers, (iii) both the dominant y scale and the time period increase, and (iv) the amplitude of the eddies decreases, and the strength of meanders increases. The energy conversion is primarily baroclinic for all the solutions. It increases by a factor 70 going from $\mathrm{Rd}_1 = 200$ km to 40 km. This is consistent with both the stronger fluctuations and the enhanced downward eddy momentum transfer by the isopycnal form stress. It is interesting that the tendency of the y scale to increase with decreasing Rd_1 is opposite to that of the marginal eigenmode (see section 3d and appendix B). This suggests that the linear analysis fails at this point.

d. Free-slip boundary condition

How does the dynamics depend upon the lateral boundary condition? Like in section 4b, we calculate a sequence of solutions with the free-slip boundary and increasing transport (10). Here V_0 has values of 0.5, 0.7, 0.9, 1.1, 1.3, 1.5, and 1.7 m s^{-1} (see Table 3). In each solution, except for $V_0 = 0.7$ m s^{-1}, the flow eventually becomes periodic. For $V_0 = 0.7$ m s^{-1}, the flow is weakly chaotic with two dominant spectral peaks at 97 and 830 days. This behavior is qualitatively similar to that of the weakly chaotic no-slip solution at $V_0 = 0.42$ m s^{-1}.

Table 3 shows that the number of eddies in the domain decreases with the growing intensity of the flow; hence the spatial period increases, but the time period decreases due to faster advection. Indeed, for $V_0 > 1.1$ m s^{-1} the time period T scales advectively; that is, $[T] = \delta_M V_0^{-1}$, as well as for the critical eigenmode of the underlying steady state (see section 3g), but it is 3.8 times longer than the eigenmode period. The y wavelength of

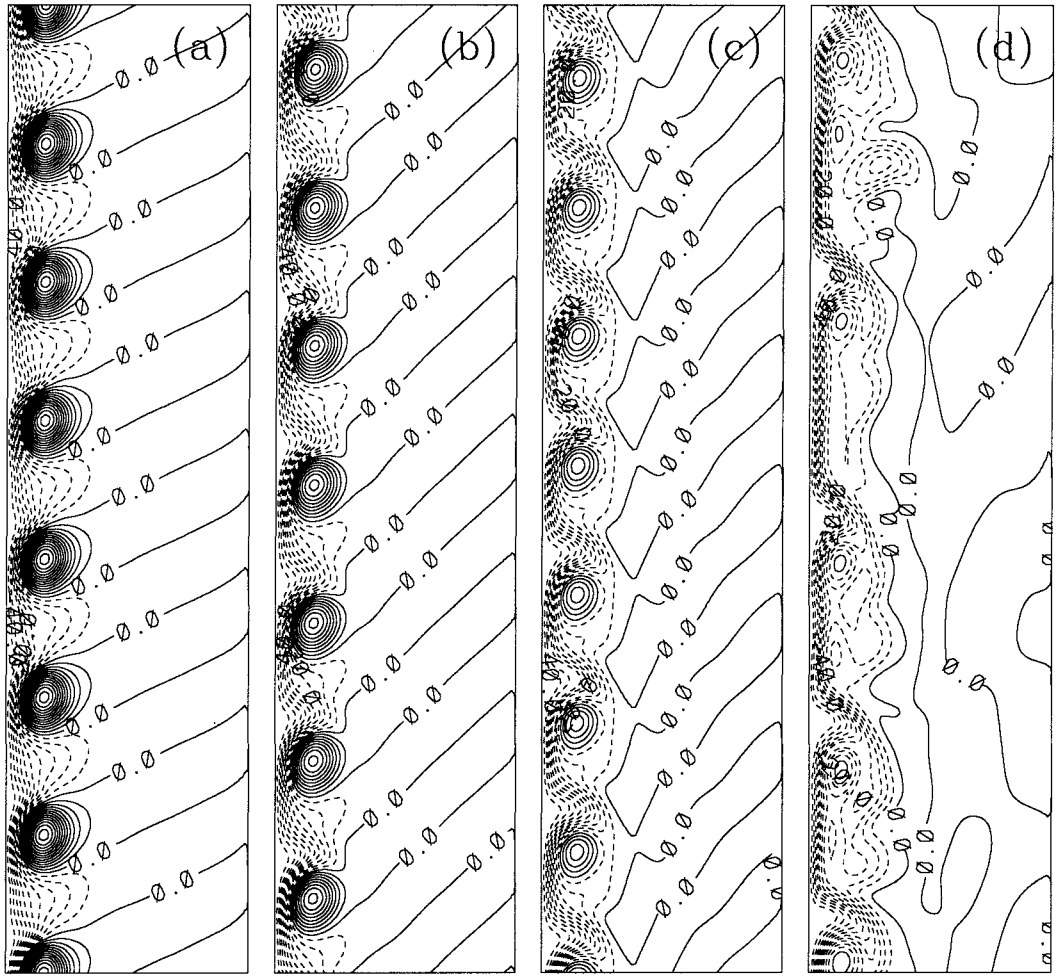

FIG. 11. ψ_1 for the no-slip solutions with $V_0 = 1.0$ m s^{-1} and $\nu = 500$ m^2 s^{-1}; Rd$_1$ equal to (a) 200, (b) 90, (c) 60, and (d) 40 km (CI = 5×10^3). Only one-half of the channel period is shown.

the nonlinear perturbation is about 2 times longer than that of the linear eigenmode. All this suggests that, although the time-mean velocity of the free-slip flow is rather close to the corresponding steady state (see Fig. 13 for $V_0 = 1.7$ m s^{-1}), the perturbation differs substantially from the most unstable eigenmode of the steady state.

The free-slip equilibrium flow is much more stable and regular at large V_0 than the no-slip one (section 4b).

TABLE 3. Change in time period and number of eddies of free-slip solution for varying V_0.

V_0 (m s^{-1})	Time period (days)	Number of eddies
0.5	121	11
0.7	97	10
0.9	94	7
1.1	86	7
1.3	80	5
1.5	74	5
1.7	68	5

The deep flow structure at $V_0 = 0.9$ m s^{-1} is shown in Fig. 12, and it can be compared with the no-slip deep flow in Fig. 8. With the free-slip boundary, the deep flow is very weak. The energy conversion is still primarily baroclinic, but at $V_0 = 1.7$ m s^{-1} it is 6 times smaller than that with the same transport but with the no-slip boundary. All this indicates that as intensity of the flow increases, the differences between the nonlinear no- and free-slip perturbations increase, and the latter favor a nonturbulent motion.

e. Multiple attractors

Do multiple attractors exist for the kind of time-dependent nonlinear solutions described in section 4? We carry out a series of integrations with different initial conditions, $\nu = 500$ m^2 s^{-1}, Rd$_1 = 52$ km, and $V_0 = 1.0$ m s^{-1}. In this case a limit cycle solution contains 15 equally spaced eddies over the period of the channel. Possibly, there are stable attractors with different numbers of eddies, but we have not yet found any. However,

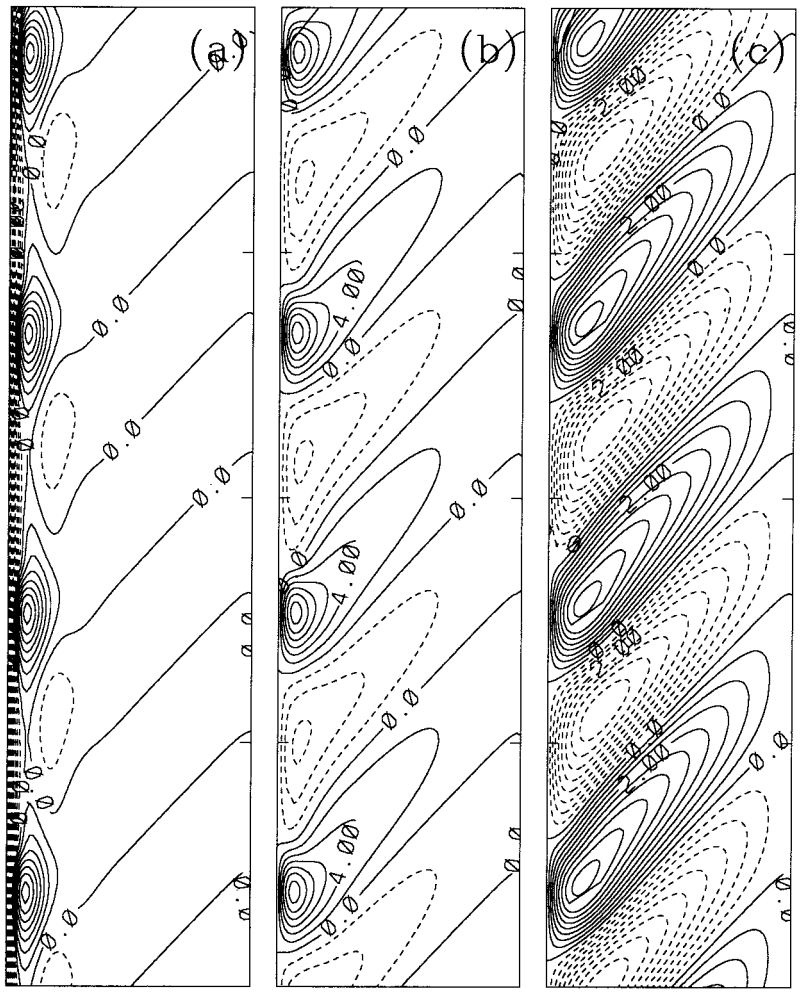

FIG. 12. Free-slip solution for $\nu = 500$ m^2 s^{-1}, $\mathrm{Rd}_1 = 52$ km, and $V_0 = 0.9$ m s^{-1}: (a) ψ_1 (CI $= 5 \times 10^3$), (b) ψ_2 (CI $= 2 \times 10^3$), and (c) ψ_3 (CI $= 0.5 \times 10^3$). Only one-half of the channel period is shown.

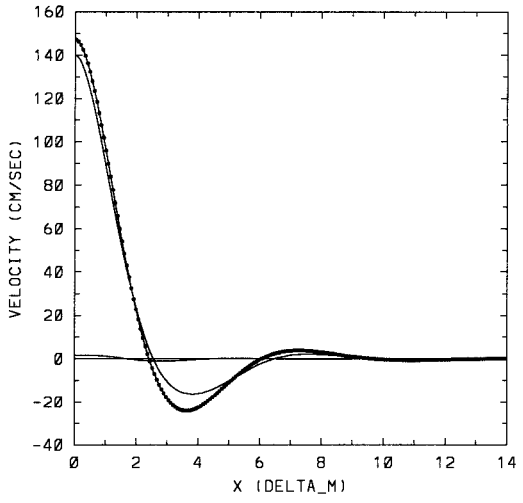

FIG. 13. As in Fig. 9 but for free-slip boundary condition.

we do find the weakly chaotic attractors shown in Fig. 14. They have eddy sequences interspersed with ''defects,'' that is, with intervals of the WBC that are almost parallel to the wall. There are different combinations of the defects in each attractor.

The local WBC dynamical system may contain many stable and unstable attractors with different sequences of eddies and defects. We have not attempted to map them comprehensively. From just these few examples, though, we can draw some important conclusions about the system. First, all the attractors that we find are qualitatively similar since the differences arise only in the particular ordering of the spatial elements. Second, motion on the attractors exhibits a large degree of the low-frequency variability associated with infrequent defects. In a more general situation, it is likely that the system will wander around the underlying skeleton of attractors, therefore it will exhibit different spatiotemporal patterns in different epochs. The question of whether the gyre-scale circulation, like the local model, contains regimes

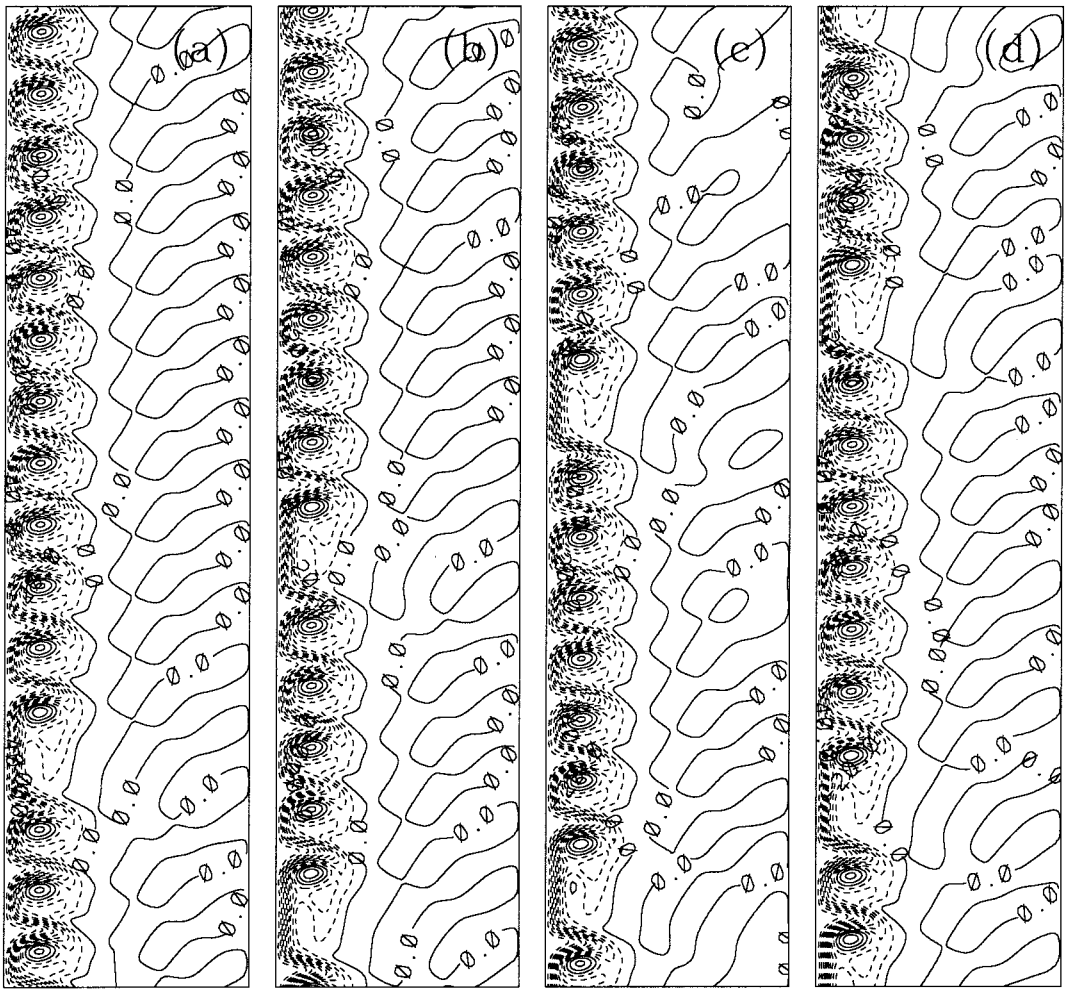

FIG. 14. No-slip solutions with $\nu = 500$ m^2 s^{-1}, $\mathrm{Rd}_1 = 52$ km, and $V_0 = 1.0$ m s^{-1} (CI $= 5 \times 10^3$). Each solution is obtained by starting from a different initial condition.

with different eddy patterns inside the WBCs remains to be explored.

5. Conclusions

We have explored the linear stability and nonlinear time evolution for the local, meridionally homogeneous, quasigeostrophic dynamics of a western boundary current (WBC) with steady transport for a wide range of parameters. Also, we illustrated that a strongly unstable WBC of the wind-driven double-gyre circulation is associated with a very broad eastward jet and absence of the intense recirculation zones, similar to what was observed by Haidvogel et al. (1992). Our principal conclusions are the following:

1) The steady WBC loses stability at moderate Reynolds numbers, Re.
2) The marginal stability threshold strongly depends upon the stratification profile of the WBC and it has a primarily baroclinic conversion in the regime that we focus on.
3) The linear instability mode has a structure that is rather different from the finite amplitude perturbations at large Re in the range of our exploration.
4) The flow reaches a periodic state for a wide intermediate range of Re.
5) The periodic and turbulent flows contain well-defined mesoscale eddies with adjacent meanders, especially in the no-slip situation.
6) The thickness of the time-mean no-slip boundary layer increases with Re; the near-wall (sublayer) velocity shear of the linear instability mode also increases with Re.
7) There are multiple stable equilibria for the local dynamics.
8) The dynamics of the WBC is fundamentally different in the no-slip and free-slip situations. The free-slip condition has a stabilizing effect on the flow in the nonlinear regime.

9) The group velocities of the least stable WBC eigenmodes are consistently larger in the free-slip than in the no-slip situation. This suggests that the latter is more apt to be disrupted by disturbances.
10) The dynamical regimes of the basin-scale circulation are different when the WBC is either stable or unstable.

The marginal stability problem yields critical eigenmodes that are trapped near the western boundary and possess decaying oscillatory tails. This is similar to what was observed by Ierley and Young (1991) in the barotropic situation. In comparison with the barotropic WBC, the 3D stability threshold moves to substantially lower Re, and the linear instability mechanism becomes essentially baroclinic in the explored wide range of parameters. The critical linear eigenmode is surface intensified. Typically, it has a time period of several months and a longitudinal wavelength of several hundred kilometers, and its phase speed is about 0.05 m s^{-1}, which is much smaller than the maximum velocity of the mean flow. For smaller ν or weaker stratification (e.g., smaller deformation radius, Rd_1, or less sharp thermocline), the marginal instability occurs for a weaker mean flow.

The nonlinear, time-dependent WBC exhibits a variability pattern that, with increasing total transport, deviates rapidly from the linear instability eigenmode of the underlying steady state. With no-slip lateral boundary condition, in the Re neighborhood of the primary instability threshold, we see weakly chaotic or quasiperiodic solutions followed, in a range of larger Re, by periodic solutions. This transitional behavior remains to be explained, but analogous behavior was found in the baroclinic wind-driven gyre circulation for a certain range of supercritical Re (Berloff and Meacham 1998a). In the gyre circulation, as Re is increased, there are chaotic states that cease to exist at some point. Beyond this point the circulation becomes periodic with an orderly generation of eddies in the boundary current.

The typical, no-slip, periodic or weakly chaotic pattern consists of a sequence of eddies propagating along the western boundary. There is a propagating meander in front of each eddy. The longitudinal size of each element containing the eddy, meander, and the adjacent portion of the WBC is several hundred kilometers. This is slightly larger than the y wavelength of the most unstable eigenmode of the underlying steady state. The time for the element's passage is about several months. This time is substantially larger than that of the most unstable eigenmode. When the total transport is increased, the flow, eventually, becomes turbulent. The dominant energy conversion between the mean state and perturbations is always baroclinic in the range of explored parameters. Compared to the underlying steady state, the time-mean flow has smaller velocity near the western wall, a substantially weaker counterflow, and a much stronger jet eastward from the counterflow. The effects of reducing the first baroclinic deformation radius (keeping the interfacial density jumps equal) are better excitation of the flow in deep layers, a decrease of the eddy amplitude, and an increase of the meander amplitude. These changes are due to the enhanced baroclinic instability of the flow.

The WBC dynamics is fundamentally different in the no- and free-slip situations. The steady free-slip flow is slightly more stable than the no-slip one. In the former case the eigenmode decays slower away from the western boundary. The group velocity of the linear free-slip eigenmode is substantially larger than that of the no-slip one. Therefore, in the former situation, a perturbation envelope exits a finite domain faster, thus contributing to the relative stability of the WBC. With the free-slip boundary condition, the WBCs with significantly supercritical transport remain periodic or nearly periodic for a very wide range of Re. Even with the largest transport examined, the solution does not reach a turbulent regime and its time mean never substantially deviates from the underlying steady state. Since the model boundary conditions are subgrid-scale parameterizations of the true turbulent processes near the boundary, they may even be considered as the extremes of a partial-slip parameterization with a single adjustable parameter (Haidvogel et al. 1992). Since at least some oceanic WBCs (along the U.S. East Coast, for example) seem neither to be stable nor to be extremely disrupted by eddies, our results suggest that a partial-slip parameterization may be the most appropriate one, although other effects (e.g., sloping topography or a coastline tilted from the north–south direction) may account for this.

The WBCs in the local model can have a variety of stable multiple equilibria that are rather similar among themselves. Each equilibrium is characterized by a specific sequence of the eddy and meander elements interspersed with sparse defects. Each equilibrium has a certain amount of low-frequency variability associated with the infrequent arrival of the defects. In the presence of stochastic forcing, another low-frequency variability may arise as a result of transitions between such equilibria. It remains to be explored whether the gyre circulation may experience transitions between metastable states characterized by different eddy sequences in the WBC. At even larger Re, where the flow is chaotic and, so far, we find no evidence of multiple equilibria, frequency spectra show that most of the total energy variability occurs in the interannual band, but the power gradually shifts to higher frequencies as intensity of the flow grows.

The dynamical regimes of the wind-driven gyre circulation can be quite different in the situations with and without instabilities in the WBCs. The situation with stable WBCs corresponds to the time-mean flow with the dipole structure of the western recirculation zones (e.g., Holland 1978) with low-frequency variability of

the type analyzed by Berloff and McWilliams (1999). The unstable WBCs correlate with the double-jet circulation regime (Fig. 1), although what is the role of boundary instabilities and transient eddies in global changes of the gyre circulation remains to be understood.

Gyre dynamics with a strongly unstable WBC has not yet been extensively studied because the large values of Re necessary for the instability to occur have rarely been achieved. Under the assumption that the WBC dynamics and the global dynamics of the gyre are significantly coupled, our results suggest further systematic studies of both the local and coupled dynamics with some new physics brought into consideration. The new physics is to include alternative forms for the frictional subgrid-scale operators and their associated boundary conditions, variations in the bottom topography and coastline position, and nonquasigeostrophic effects, such as outcropping, that is, intersection of the isopycnals with the domain boundaries.

Acknowledgments. Funding for this research was provided by the National Science Foundation Grant OCE-96-33681 and by the Office of Naval Research Grant N00014-98-1-0165. We thank the anonymous reviewers for careful and constructive reviews.

APPENDIX A

Asymptotic Behavior at Large and Small Viscosity

We consider solutions of (11) in the asymptotic limits

$$\nu \to \infty \tag{A1}$$

and

$$\nu \to 0. \tag{A2}$$

Because $\delta_M \sim \nu^{1/3}$ in the limit (A1), the WBC is very wide, and in the limit (A2) it is very narrow in comparison with Rd_1. The limit (A1) is unrealistic because the WBC width becomes of the size of the ocean. In the limit (A2) the flow is turbulent, and, therefore, the linear analysis may be useless. Nevertheless, exploring the extremes helps to analyze solutions with moderate values of ν, that is, WBCs that are both realistic and moderately turbulent as in modern GCMs. Our goal is to find proper scales and balances of (11) in both limit (A1) and limit (A2).

We assume that the interior transport in the gyre is constant and that it is balanced by the WBC transport (10). Therefore, the streamfunction scale, $[\psi] = \psi_0 = V_0\delta_M$, is constant and the Reynolds number is

$$\mathrm{Re} = \frac{\psi_0}{\nu} \sim \nu^{-1}. \tag{A3}$$

We introduce the time, $[T]$, and length, $[L]$, scales which will be specified below. The velocity scale, $[\overline{U}] = \psi_0\delta_M^{-1}$, comes from the steady-state velocity. The channel width is assumed to be proportional to δ_M, as in section 3; that is, $L_x = 30\delta_M$. The governing system of equations (11) yields the following scalings for the upper layer:

$$\text{(a)} \quad \frac{\partial}{\partial t}\nabla^2\psi_1 \Rightarrow \psi_0[T]^{-1}L^{-2}$$

$$\text{(b)} \quad -S_{1,2}\frac{\partial}{\partial t}(\psi_1 - \psi_2) \Rightarrow \psi_0[T]^{-1}\mathrm{Rd}_1^{-2}$$

$$\text{(c)} \quad \overline{v}_1\frac{\partial}{\partial y}\nabla^2\psi_1 \Rightarrow [\overline{U}]\psi_0\delta_M^{-2}[L]^{-1}$$

$$\text{(d)} \quad \overline{v}_1 S_1\frac{\partial\psi_2}{\partial y} \Rightarrow [\overline{U}]\psi_0\mathrm{Rd}_1^{-2}[L]^{-1}$$

$$\text{(e)} \quad -\overline{v}_{1xx}\frac{\partial\psi_1}{\partial y} \Rightarrow [\overline{U}]\psi_0[L]^{-3}$$

$$\text{(f)} \quad \beta\frac{\partial\psi_1}{\partial x} \Rightarrow \beta\psi_0[L]^{-1}$$

$$\text{(g)} \quad \nu\nabla^4\psi_1 \Rightarrow \nu\psi_0[L]^{-4}. \tag{A4}$$

Similar scaling is done for the other layers. The energy conversion integrands (17) have the following scalings:

$$\mathrm{Bt} \Rightarrow \psi_0^3[L]^{-4} \qquad \mathrm{BCL} \Rightarrow \psi_0^3[L]^{-2}\mathrm{Rd}_1^{-2}; \tag{A5}$$

therefore we expect that the baroclinic conversion dominates in the limit (A1) because $[L] \to \infty$. Also, we expect that the barotropic conversion dominates in the limit (A2) because $[L] \to 0$. Since (A5) is merely a scale estimate, it does not say whether there is any instability. In the following we consider the limits (A1) and (A2) separately.

a. Large viscosity

In this limit all the eigenmodes are stable. The natural length scale is $[L] = \delta_M \sim \nu^{1/3}$. The leading terms in (A4) are (f) and (g). For time-dependence assumed by the linear stability analysis, the leading terms must be supplemented and balanced by one of the first two terms in (A4). The proper balance can be achieved when $[T] \sim \nu^{1/3}$. We find $[T] = \delta_M[U]^{-1} = \delta_M\beta^{-1}\mathrm{Rd}_1^{-2}$ by using the phase speed of a long baroclinic Rossby wave as the appropriate velocity scale. The scale for $[T]$ is shorter than the advective scale $\psi_0^{-1}\delta_M^2 \sim \nu^{2/3}$. The steady-state velocity does not enter the leading balance, therefore the eigenmodes are uncoupled from the steady state. The solutions are baroclinic, viscous channel modes satisfying

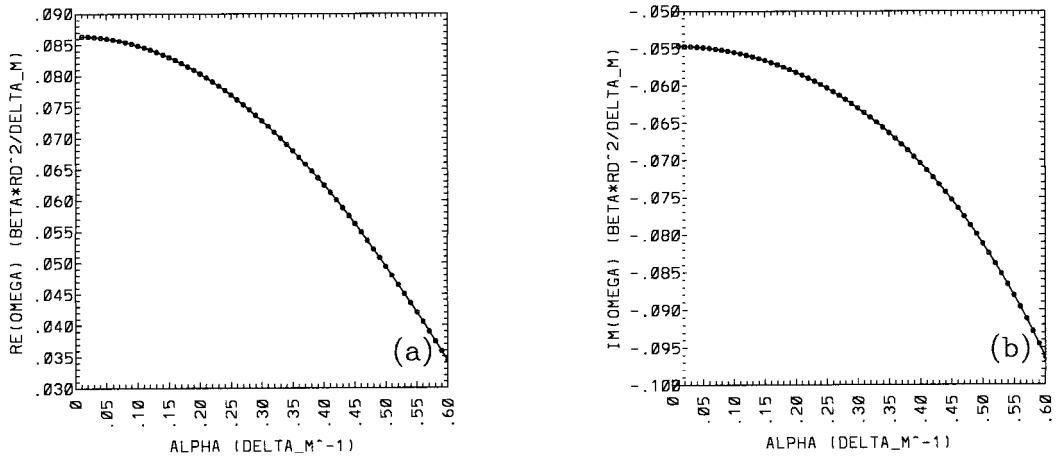

FIG. A1. (a) Eigenfrequency and (b) growth rate of the least stable no-slip eigenmodes as functions of α ($\nu \to \infty$).

$$S_{1,2}\frac{\partial}{\partial t}(\psi_2 - \psi_1) + \beta\frac{\partial}{\partial x}\psi_1 = \nu\nabla^4\psi_1$$

$$S_{2,1}\frac{\partial}{\partial t}(\psi_1 - \psi_2) - S_{2,2}\frac{\partial}{\partial t}(\psi_2 - \psi_3) + \beta\frac{\partial}{\partial x}\psi_2 = \nu\nabla^4\psi_2$$

$$S_{3,1}\frac{\partial}{\partial t}(\psi_2 - \psi_3) + \beta\frac{\partial}{\partial x}\psi_3 = \nu\nabla^4\psi_3. \quad \text{(A6)}$$

The modes are different from the normal modes in the closed basin (Pedlosky 1987) because of two aspects. First, there are no latitudinal boundaries in the channel, and this leads to continuum of wave numbers in y. Second, the modes are fundamentally viscous; that is, friction is important throughout the channel.

We solve the eigenproblem (A6) with boundary conditions (14) and (15) numerically, as in section 3. The eigenfrequencies Re(ω) (Fig. A1a) and the growth rates Im(ω) (Fig. A1b), in the limit (A1) converge to universal dependencies on α. The growth rates are the largest, although always negative, at $\alpha \to 0$, therefore we expect that small amplitude perturbations with large y-scale are the last to decay. The dispersion curve in Fig. A1a becomes flat in the limit $\alpha \to 0$ indicating that the group velocity c_g vanishes. As a consequence of this an envelope of the slowest decaying perturbations does not move away as happens at moderate values of ν (section 3e) or in the limit (A2). There are only negligible differences between $\omega(\alpha)$ calculated with either (15a) or (15b) boundary conditions. The viscous channel modes in the limit (A1) are less confined to the western part of the channel than the critical modes (e.g., Fig. 5) found at moderate values of ν. The no-slip modes in the limit (A1) (Fig. A2) are somewhat less confined than the free-slip modes (not shown), but both look qualitatively similar.

It is obvious that in the limit (A1) the energy conversion between the eigenmodes and the mean flow vanishes asymptotically, and it is dominated by BCL.

b. Small viscosity, no-slip boundary

In this limit it is expected that some of the eigenmodes are unstable. If we take

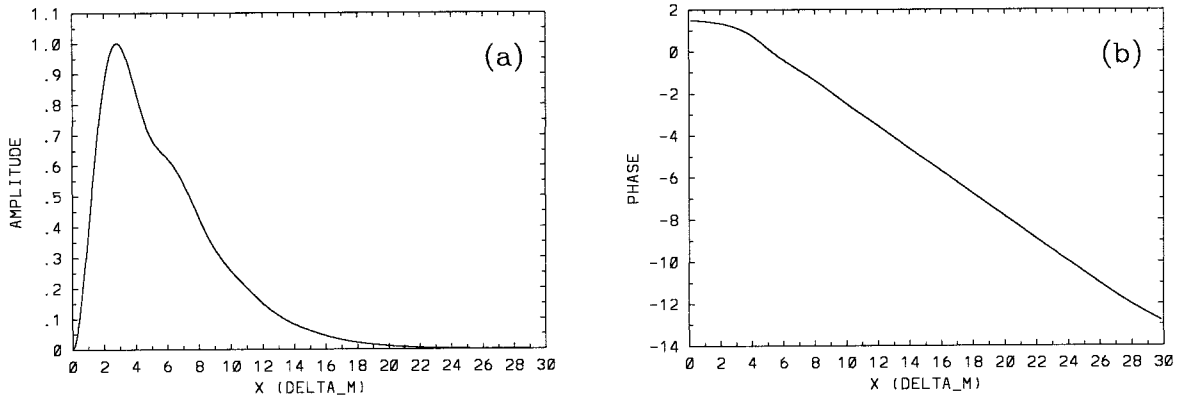

FIG. A2. (a) Amplitude and (b) phase of the least stable no-slip eigenmode for $\alpha = 0.01\delta_M^{-1}$ ($\nu \to \infty$).

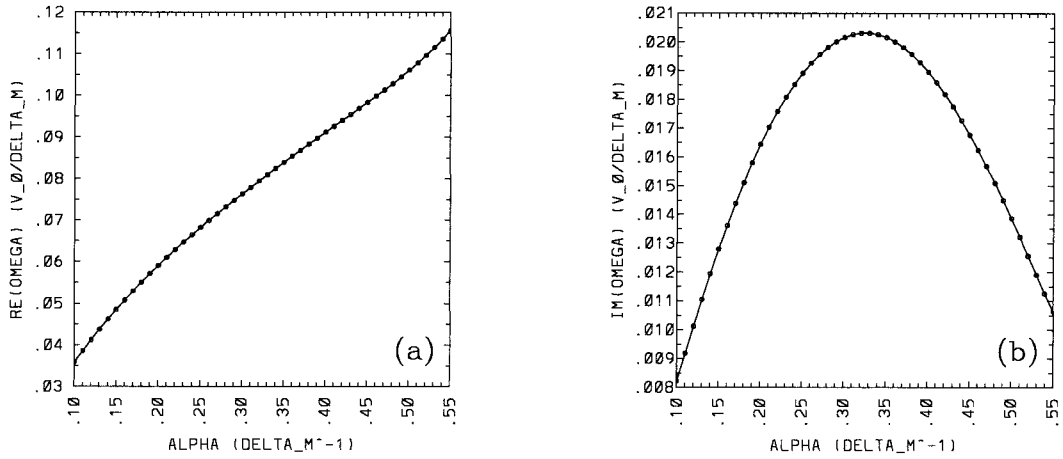

FIG. A3. (a) Eigenfrequency and (b) growth rate of the most unstable no-slip eigenmode as functions of α ($\nu \to 0$).

$$[L] = \delta_M \sim \nu^{1/3}, \tag{A7a}$$

then the leading terms in (A4) become (c) and (e). The balance with one of the first two terms in (A4) is achieved when $[T] \sim \nu^{2/3}$. We find

$$[T] = \delta_M^2 \psi_0^{-1} \sim \nu^{2/3}, \tag{A7b}$$

that is an advective time scale. In the limit (A2) the first equation from (11) reduces to

$$\frac{\partial}{\partial t}\nabla^2\psi_1 + \overline{v}_1\frac{\partial}{\partial y}\nabla^2\psi_1 - \overline{v}_{1xx}\frac{\partial \psi_1}{\partial y} = 0, \tag{A8}$$

where each term is proportional to $\nu^{-4/3}$. The isopycnal form stresses associated with parameters $S_{i,j}$ do not enter the main balance (A8), therefore the upper layer is decoupled from the deep layers and $\psi_2 = \psi_3 = 0$. The viscous term drops out, and, as a consequence, (A8) does not satisfy the no-slip boundary condition (15a). This is especially true near the western boundary, provided that the eastern boundary is sufficiently far away. The offset can be corrected if we account for a viscous sublayer narrower than $[L] = \delta_M$.

Let us derive a scaling similar to (A4) using the sublayer length scale $[L]$, which will be specified below. By matching the inner solution with the interior solution, we find $[T] = \delta_M^2\psi_0^{-1}$. The steady-state velocity is

$$v_1 = [\overline{U}]\frac{[L]}{\delta_M}. \tag{A9}$$

The additional multiplier $[L]\delta_M^{-1}$ appears because of the first-order term, $\overline{v}_1 \sim x\delta_M^{-1}$, in the Taylor expansion near the western boundary. Now the sublayer terms scale as the following:

$$\text{(a)} \quad \frac{\partial}{\partial t}\nabla^2\psi_1 \Rightarrow \psi_0^2\delta_M^{-2}[L]^{-2} \sim [L]^{-2}\nu^{-2/3}$$

$$\text{(b)} \quad -S_{1,2}\frac{\partial}{\partial t}(\psi_1 - \psi_2) \Rightarrow \psi_0^2\delta_M^{-2}\mathrm{Rd}_1^{-2} \sim \nu^{-2/3}$$

$$\text{(c)} \quad \overline{v}_1\frac{\partial}{\partial y}\nabla^2\psi_1 \Rightarrow \psi_0^2\delta_M^{-2}[L]^{-2} \sim [L]^{-2}\nu^{-2/3}$$

$$\text{(d)} \quad \overline{v}_1 S_1\frac{\partial \psi_2}{\partial y} \Rightarrow \psi_0^2\delta_M^{-2}\mathrm{Rd}_1^{-2} \sim \nu^{-2/3}$$

$$\text{(e)} \quad -\overline{v}_{1xx}\frac{\partial \psi_1}{\partial y} \Rightarrow \psi_0^2\delta_M^{-3}[L]^{-1} \sim [L]^{-1}\nu^{-1}$$

$$\text{(f)} \quad \beta\frac{\partial}{\partial x}\psi_1 \Rightarrow \beta\psi_0[L]^{-1} \sim [L]^{-1}$$

$$\text{(g)} \quad \nu\nabla^4\psi_1 \Rightarrow \nu\psi_0[L]^{-4} \sim \nu[L]^{-4}. \tag{A10}$$

The viscous term (*g*) enters the balance with (a) if $[L] \sim \nu^{5/6}$. This implies that the viscous length scale is

$$[L] = \delta_M \mathrm{Re}^{-1/2}. \tag{A11}$$

The term (e) is relatively small; it is of an order $\nu^{-11/6}$. Thus, at large Re, that is, in the limit (A2), the sublayer is a small fraction of δ_M with the dynamics governed by the equation

$$\frac{\partial}{\partial t}\nabla^2\psi_1 + \overline{v}_1\frac{\partial}{\partial y}\nabla^2\psi_1 = \nu\nabla^4\psi_1, \tag{A12}$$

where each term is of order $\nu^{-7/3}$. The solutions of (A12) must satisfy the boundary conditions (14) and (15a), and they must asymptotically match the solutions of (A8) on the interior side of the sublayer.

The equation (A8) is solved numerically using the boundary condition (14). The growth rate $\mathrm{Im}(\omega)$ has its maximum at $\alpha = 0.33\delta_M^{-1}$ (Fig. A3b) that corresponds to the fastest growing eigenmode. The eigenmode (Fig.

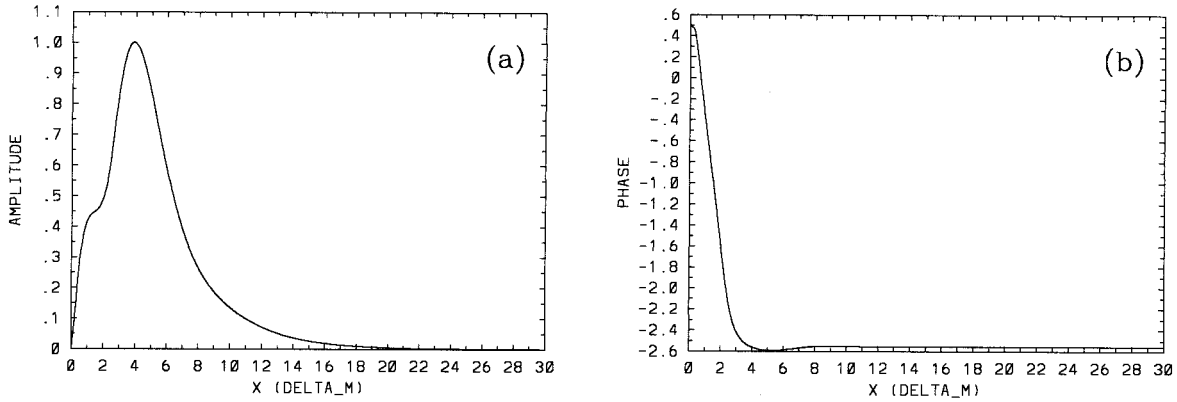

FIG. A4. (a) Amplitude and (b) phase of the most unstable no-slip eigenmode satisfying (A8) ($\nu \to 0$).

A4) has $\mathrm{Re}(\omega) = 0.079\psi_0\delta_M^{-2}$ (Fig. A3b), and the group velocity $c_g = 0.15\psi_0\delta_M^{-1}$. The phase is constant when sufficiently far away from the western boundary. This indicates that there is no propagating component in the far field. The sublayer is accounted for by solving (A8) with the viscous term on the rhs and with the no-slip boundary condition (15a). Then, in the limit (A2), the fastest growing eigenmode approaches the interior solution (Fig. A4) everywhere except for the narrow sublayer.

We emphasize that the eigenmodes of the no-slip WBC, at large Re, require fine resolution with the grid size $\Delta x \sim \nu^{5/6}$ near the western boundary. In the linear analysis, the underresolving corrupts only the sublayer structure, and it does not affect the interior solution. In the nonlinear WBC and, especially in the wind-driven gyres, when ν is small enough, the flow may be sensitive to the sublayer processes. In particular, the sublayer is a region with the largest absolute values of the relative vorticity. This vorticity is likely to be ripped away from the wall by disturbances and then to be advected in the basin interior by the eastward jet. Its further evolution may be associated with generation of coherent vortices (e.g., the Gulf Stream rings). This is an important issue that requires extensive numerical experiments and further analysis of the gyre circulation at much lower values of ν than in this paper.

c. Small viscosity, free-slip boundary

In the free-slip case, we assume that $[T]$ is advective scale (A7b), and $[L]$ is the viscous scale from (A7a). This leads to the same interior balance (A8) as in the no-slip situation, but the boundary condition changes from (15a) to (15b). The normal mode solution (12) of (A8) yields equation

$$-\omega\tilde{\psi}_{1xx} + \overline{v}_1(-\alpha^3\tilde{\psi}_1 + \tilde{\psi}_{1xx}) - \alpha\overline{v}_{1xx}\tilde{\psi}_1 = 0 \tag{A13}$$

that satisfies both boundary conditions (14) and (15b). This implies that there is no western boundary sublayer with the dynamical balance different from (A8).

APPENDIX B

Asymptotic Behavior at Small Rd_1

The first baroclinic deformation radius is defined as

$$\mathrm{Rd}_1 = U^{1/2}\beta^{-1/2}, \tag{B1}$$

where U is the phase speed of the fastest, large-scale, nonbarotropic vertical mode of the inviscid and unforced quasigeostrophic equations of motion:

$$-S_{1,2}\frac{\partial}{\partial t}(\psi_1 - \psi_2) + \beta\frac{\partial\psi_1}{\partial x} = 0$$

$$\frac{\partial}{\partial t}[-S_{2,1}(\psi_2 - \psi_1) - S_{2,2}(\psi_2 - \psi_3)] + \beta\frac{\partial\psi_2}{\partial x} = 0$$

$$S_{3,1}\frac{\partial}{\partial t}(\psi_2 - \psi_3) + \beta\frac{\partial\psi_3}{\partial x} = 0. \tag{B2}$$

We define the following parameters:

$$R_{1,2} = \frac{H_1}{H_2}, \qquad R_{1,3} = \frac{H_1}{H_3}, \qquad \gamma = \frac{\rho_2 - \rho_1}{\rho_3 - \rho_2}, \tag{B3}$$

and notice that

$$S_{2,1} = R_{1,2}S_{1,2}, \qquad S_{2,2} = \gamma R_{1,2}S_{1,2},$$
$$S_{3,1} = \gamma R_{1,3}S_{1,2}. \tag{B4}$$

The normal mode solution (12) of (B2) yields the dispersion relationships for one barotropic and two baroclinic modes. The fastest, that is, the first, baroclinic mode satisfies

$$\omega = -\beta\alpha c^2 S_{1,2}^{-1}, \tag{B5}$$

where

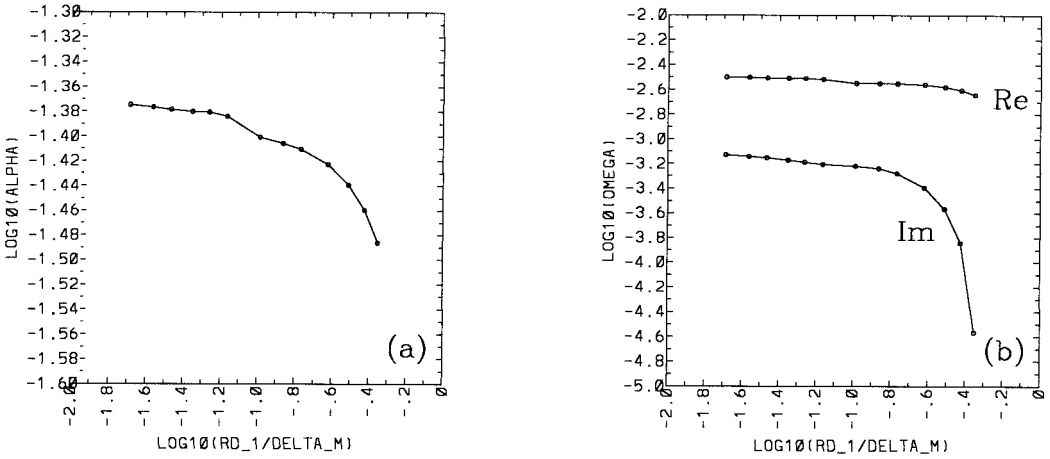

FIG. B1. (a) α and (b) ω as functions of $\mathrm{Rd}_1\delta_M^{-1}$. The length scale is $[L] = \mathrm{Rd}_1^{2/3}\delta_M^{1/3}\mathrm{Re}^{-1/3}$, and the timescale is $[T] = \mathrm{Rd}_1^{2/3}\delta_M^{4/3}\nu^{-1}\mathrm{Re}^{-4/3}$.

$$c^2 = \frac{A_1 + (A_1^2 - 4\gamma A_2)^{1/2}}{2\gamma A_2}, \tag{B6a}$$

$$A_1 = 1 + (1 + \gamma)R_{1,2} + \gamma R_{1,3},$$

$$A_2 = R_{1,2} + R_{1,3} + R_{1,2}R_{1,3}. \tag{B6b}$$

The phase speed is $U = |\omega\alpha^{-1}|$. Using (B1) we obtain

$$S_{1,2} = c^2\mathrm{Rd}_1^{-2}. \tag{B7}$$

We consider $R_{1,2}$, $R_{1,3}$, and γ to be constant; therefore c is constant. In the limit $\mathrm{Rd}_1 \to 0$: $S_{i,j} \sim \mathrm{Rd}_1^{-2}$, and from (B4) and (B7) it follows that

$$S_{1,2} = c^2\mathrm{Rd}_1^{-2}, \qquad S_{2,1} = R_{1,2}c^2\mathrm{Rd}_1^{-2},$$

$$S_{2,2} = \gamma R_{1,2}c^2\mathrm{Rd}_1^{-2}, \qquad S_{3,1} = \gamma R_{1,3}c^2\mathrm{Rd}_1^{-2}. \tag{B8}$$

Given $\mathrm{Rd}_1 \to 0$, the leading order balances in (11) are

$$-S_{1,2}\frac{\partial}{\partial t}(\psi_1 - \psi_2) + S_{1,2}\overline{v}_1\frac{\partial \psi_2}{\partial y} = 0$$

$$\frac{\partial}{\partial t}[-S_{1,2}(\psi_2 - \psi_1) - S_{2,2}(\psi_2 - \psi_3)] - S_{2,1}\overline{v}_1\frac{\partial \psi_2}{\partial y} = 0$$

$$S_{3,1}\frac{\partial}{\partial t}(\psi_2 - \psi_3) = 0. \tag{B9}$$

The system (B9) satisfies none of the boundary conditions (15). The last equation in (B9) implies $\psi_2 = \psi_3$, therefore the first and second equations are identical. This implies that the system (B9) is degenerate, and we have to bring in the next important term, $\nu\nabla^4\psi_i$, in order to get rid of the degeneracy. In the limit $\mathrm{Rd}_1 \to 0$, and after some rearrangements, the expanded governing equations become

$$\frac{\partial}{\partial t}(\psi_2 - \psi_1) + \overline{v}_1\frac{\partial \psi_2}{\partial y} = \nu S_{1,2}^{-1}\nabla^4\psi_1$$

$$\frac{\partial}{\partial t}(\psi_1 - \psi_2) + \frac{S_{2,2}}{S_{2,1}}\frac{\partial}{\partial t}(\psi_3 - \psi_2) = \nu S_{2,1}^{-1}\nabla^4\psi_2$$

$$\nabla^4[S_{1,2}^{-1}\psi_1 + S_{2,1}^{-1}\psi_2 + S_{2,2}(S_{2,1}S_{3,1})^{-1}\psi_3] = 0. \tag{B10}$$

When the last equation is combined with the boundary conditions (14) and (15), the expression in brackets, that is, the barotropic streamfunction, is zero everywhere; hence in terms of the parameters in (B3) we have

$$\psi_3 = -R_{1,3}\psi_1 - R_{1,3}R_{1,2}^{-1}\psi_2. \tag{B11a}$$

By using (B3), the governing equations for ψ_1 and ψ_2 become

$$\frac{\partial}{\partial t}(\psi_2 - \psi_1) + \overline{v}_1\frac{\partial \psi_2}{\partial y} = \nu\mathrm{Rd}_1^2c^{-2}\nabla^4\psi_1 \tag{B11b}$$

$$\frac{\partial}{\partial t}[-\gamma R_{1,3}\psi_1 - (1 + \gamma R_{1,3}R_{1,2}^{-1})\psi_2]$$
$$= \nu\mathrm{Rd}_1^2c^{-2}\nabla^4(\psi_1 + R_{1,2}^{-1}\psi_2). \tag{B11c}$$

Solutions of (B11) satisfy the full set of boundary conditions (14) and (15).

The governing system of equations (B11) yields the following scalings:

(a) $$\frac{\partial}{\partial t}(\psi_2 - \psi_1) \Rightarrow \psi_0[T]^{-1}$$

(b) $$\overline{v}_1\frac{\partial \psi_2}{\partial y} \Rightarrow [\overline{U}]\psi_0[L]^{-1}$$

(c) $$\nu\mathrm{Rd}_1^2c^{-2}\nabla^4\psi_1 \Rightarrow \nu\mathrm{Rd}_1^2\psi_0[L]^{-4}$$

(d) $$\frac{\partial}{\partial t}[-\gamma R_{1,3}\psi_1 - (1 + \gamma R_{1,3}R_{1,2}^{-1})\psi_2] \Rightarrow \psi_0[T]^{-1}$$

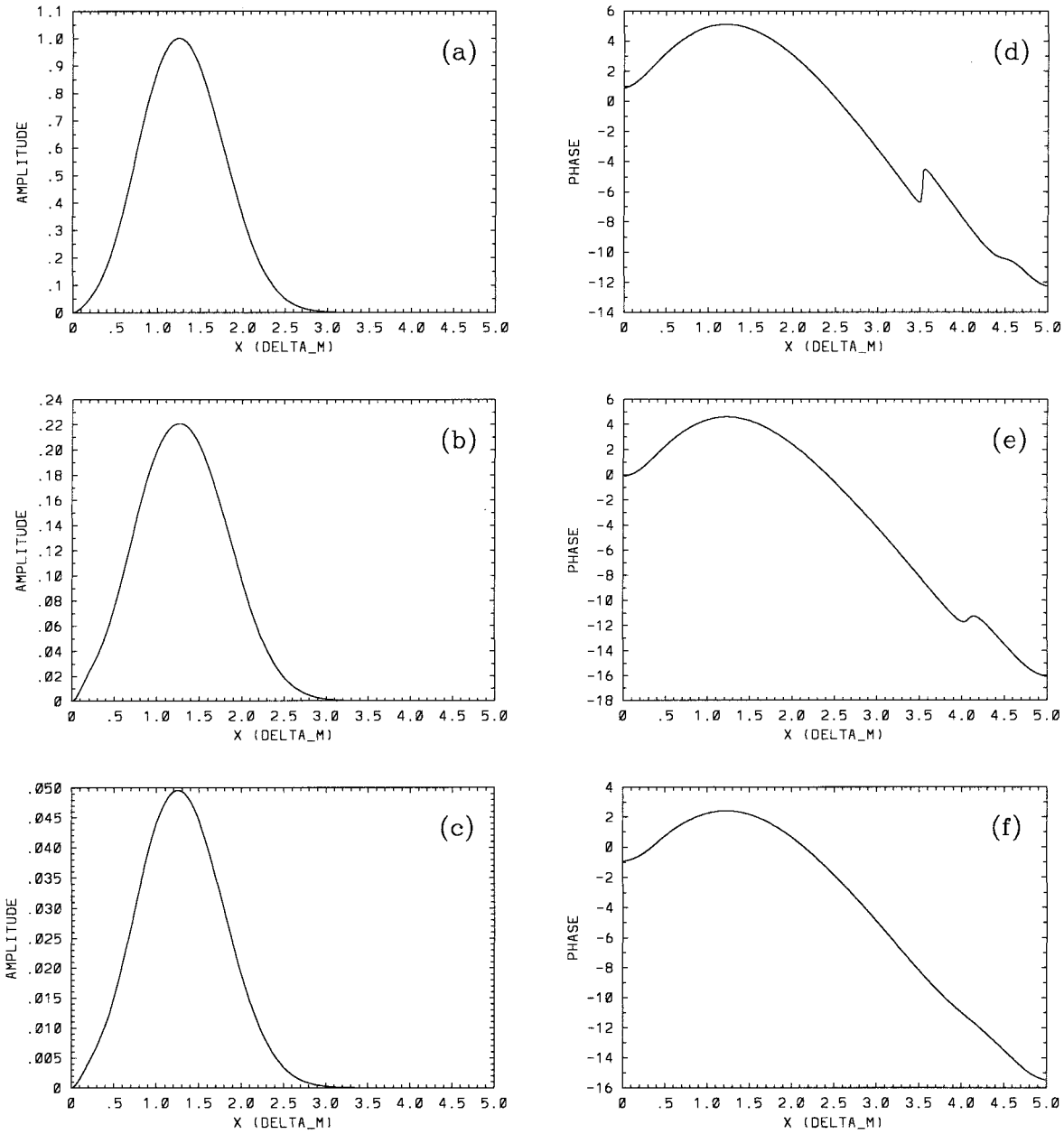

FIG. B2. Plot of the amplitude (a–c) and phase (d–f) of the no-slip fastest growing eigenmode, in the limit $\mathrm{Rd} \to 0$, obtained as the solution of (B11).

(e) $$\nu \mathrm{Rd}_1^2 c^{-2} \nabla^4 (\psi_1 + R_{1,2}^{-1} \psi_2) \Rightarrow \nu \mathrm{Rd}_1^2 \psi_0 [L]^{-4}. \quad \text{(B12)}$$

From (B12) and $[\overline{U}] = \psi_0 \delta_M^{-1}$, it follows that the appropriate time and length scales in the limit $\mathrm{Rd}_1 \to 0$ are

$$[L] = \mathrm{Rd}_1^{2/3} \delta_M^{1/3} \mathrm{Re}^{-1/3}, \qquad [T] = \mathrm{Rd}_1^{2/3} \delta_M^{4/3} \nu^{-1} \mathrm{Re}^{-4/3}. \quad \text{(B13)}$$

In order to test the scaling (B13), we numerically solve the governing equations (B11) with the no-slip boundary condition by using the normal mode decomposition and the numerical method described in section 3. We use $R_{1,2} = 3/7$, $R_{1,3} = 1/10$, and $\gamma = 1$ as in sections 2 and 3 (except section 3h). Given α and Rd_1, we find the fastest growing eigenmode. There is a single band of unstable eigenmodes in each case. We plot α and ω, scaled according to (B13), as functions of $\mu = \mathrm{Rd}_1 \delta_M^{-1}$ (Fig. B1). The figure shows that the curves flatten out at small Rd_1. This suggests that the scaling (B13) is correct. At small Rd_1, the eigenfunctions of (B11) are confined to the first maximum of the steady state (see Fig. B2), and they have

very short y wavelength and the time period, as suggested by (B13).

APPENDIX C

"Sharp Thermocline" Asymptotic Behavior

We solve (11) in the asymptotic limit $\gamma \to \infty$, which corresponds to a sharp thermocline. We assume that Re, ν, and Rd_1 have moderate values, such as in section 3. From (B6), (B7), and (B8) it follows that for large γ:

$$c^2 \sim 1, \quad S_{1,2} \sim S_{2,1} \sim 1, \quad S_{2,2} \sim S_{3,1} \sim \gamma. \tag{C1}$$

Given the viscous length scale $[L] = \delta_M$, the second and third layer balances in (11) become

$$\text{(a)} \quad \frac{\partial}{\partial t}\nabla^2\psi_{2,3} \Rightarrow \psi_0[T]^{-1}\delta_M^{-2}$$

$$\text{(b)} \quad -S_{2,1}\frac{\partial}{\partial t}(\psi_1 - \psi_2) \Rightarrow \psi_0[T]^{-1}R_{1,2}\mathrm{Rd}_1^{-2}$$

$$\text{(c)} \quad -S_{2,2}\frac{\partial}{\partial t}(\psi_3 - \psi_2) \Rightarrow \psi_0[T]^{-1}\gamma R_{1,2}\mathrm{Rd}_1^{-2}$$

$$\text{(d)} \quad S_{3,1}\frac{\partial}{\partial t}(\psi_2 - \psi_3) \Rightarrow \psi_0[T]^{-1}\gamma R_{1,3}\mathrm{Rd}_1^{-2}$$

$$\text{(e)} \quad -S_{2,1}\overline{v}_1\frac{\partial \psi_2}{\partial y} \Rightarrow \psi_0^2\delta_M^{-1}[L_y]^{-1}R_{1,2}\mathrm{Rd}^{-2}$$

$$\text{(f)} \quad \beta\frac{\partial \psi_{2,3}}{\partial x} \Rightarrow \beta\psi_0\delta_M^{-1}$$

$$\text{(g)} \quad \nu\nabla^4\psi_{2,3} \Rightarrow \nu\psi_0\delta_M^{-4}, \tag{C2}$$

where parameters $R_{i,j}$ are defined in (B3). The proper timescale is

$$[T] = \delta_M\gamma R_{1,2}\mathrm{Rd}_1^{-2}\beta^{-1} \sim \gamma, \tag{C3}$$

and it is proportional to the time scale of the first, baroclinic long Rossby wave. The terms (a) and (b) are of order $O(\gamma^{-1})$. They drop out of the main balance when $\gamma \to \infty$. At the end of this appendix, it is shown that y-scale $[L_y]$ is large, that is, $\alpha \to 0$ for the least stable modes. Therefore term (e) drops out of the main balance. As a result, the equations governing $\psi_{2,3}$ become decoupled from the upper layer equation. In the nondimensional form, these equations are

$$R_{1,2}\frac{\partial}{\partial t}(\psi_3 - \psi_2) + \frac{\partial \psi_2}{\partial x} = \nabla^4\psi_2$$

$$R_{1,3}\frac{\partial}{\partial t}(\psi_2 - \psi_3) + \frac{\partial \psi_3}{\partial x} = \nabla^4\psi_3. \tag{C4}$$

From (C4), given the boundary conditions (14) and (15), we find the prognostic equation for ψ_2:

$$-(R_{1,2} + R_{1,3})\frac{\partial \psi_2}{\partial t} + \frac{\partial \psi_2}{\partial x} = \nabla^4\psi_2, \tag{C5}$$

and the diagnostic relationship for ψ_3:

$$\psi_3 = -R_{1,3}R_{1,2}^{-1}\psi_2. \tag{C6}$$

Given ψ_2, the upper-layer perturbation ψ_1 is governed by the equation

$$\left(\nabla^4 - \frac{\partial}{\partial x} - \overline{v}_1\frac{\partial}{\partial y}\nabla^2 + \overline{v}_{1xx}\frac{\partial}{\partial y}\right)\psi_1 = R_{1,2}\left(\frac{\partial}{\partial t} + \overline{v}_1\frac{\partial}{\partial y}\right)\psi_2. \tag{C7}$$

It appears that the dynamics of the sharp thermocline ($\gamma \to \infty$) is controlled by the deep layers; that is, ω and α are set by the deep flow and ψ_1 is found diagnostically. The equation (C5) describes the dynamics of the viscous channel mode (see appendix A) with the relationship between ω and α qualitatively similar to the one shown in Fig. A1. All the modes are stable, that is, they have negative growth rates. The least stable modes correspond to $\alpha \to 0$; hence we justify that the term (e) from (C2) is indeed small, and it does not enter the main balance. It is easy to see that as $\gamma \to \infty$: both $\mathrm{Re}(\omega)$ and α decrease, and the forcing term on the right-hand side of (C7) decreases in amplitude. Therefore, the amplitude of ψ_1 becomes negligible relative to the amplitudes of ψ_2 and ψ_3.

REFERENCES

Berloff, N., and L. Howard, 1997: Solitary waves and periodic pulse trains as exact solutions for nonlinear nonintegrable systems. *Studies Appl. Math.,* **99,** 1–24.

Berloff, P. and S. Meacham, 1998a: The dynamics of a simple baroclinic model of the wind-driven circulation. *J. Phys. Oceanogr.*, **28,** 361–388.

——, and ——, 1998b: On the stability of the wind-driven circulation. *J. Mar. Res.*, **56,** 937–993.

——, and J. McWilliams, 1999: Large-scale, low-frequency variability in wind-driven ocean gyres. *J. Phys. Oceanogr.*, **29,** 2607–2634.

Blandford, R., 1971: Boundary conditions in homogeneous ocean models. *Deep-Sea Res.,* **18,** 739–751.

Bryan, K., 1963: A numerical investigation of a nonlinear model of a wind-driven ocean. *J. Atmos. Sci.*, **20,** 594–606.

Cessi, P., and G. Ierley, 1993: Nonlinear disturbances of western boundary currents. *J. Phys. Oceanogr.*, **23,** 1727–1735.

Cox, M., 1979: A numerical study of Somali Current eddies. *J. Phys. Oceanogr.*, **9,** 311–326.

Feron, R., 1995: The Southern Ocean western boundary currents: Comparison of fine resolution Antarctic model results with Geosat altimeter data. *J. Geophys. Res.*, **100,** 4959–4975.

Haidvogel, D., and W. Holland, 1978: The stability of ocean currents in eddy-resolving general circulation models. *J. Phys. Oceanogr.,* **8,** 393–413.

——, J. McWilliams, and P. Gent, 1992: Boundary current separation in a quasigeostrophic, eddy-resolving ocean circulation model. *J. Phys. Oceanogr.,* **22,** 882–902.

Holland, W., 1978: The role of mesoscale eddies in the general circulation of the ocean—Numerical experiments using a wind-driven quasigeostrophic model. *J. Phys. Oceanogr.,* **8,** 363–392.

Ierley, G., 1990: Boundary layers in the general ocean circulation. *Annu. Rev. Fluid Mech.,* **22,** 111–142.

——, and W. Young, 1991: Viscous instabilities in the western boundary layer. *J. Phys. Oceanogr.*, **21,** 1323–1332.

Ikeda, M., 1983: Linear instability of a current flowing along a bottom slope using a three-layer model. *J. Phys. Oceanogr.*, **13,** 208–223.

Munk, W., 1950: On the wind-driven ocean circulation. *J. Meteor.*, **7,** 79–93.

Pedlosky, J., 1987: *Geophysical Fluid Dynamics.* 2d ed. Springer-Verlag, 710 pp.

Sheremet, V., G. Ierley, and V. Kamenkovich, 1997: Eigenanalysis of the two-dimensional wind-driven ocean circulation problem. *J. Mar. Res.*, **55,** 57–92.

Veronis, G., 1966: Wind-driven ocean circulation. Part 2. *Deep-Sea Res.*, **13,** 31–55